

Feasibility study for an in-vivo  
scintillator-fibre dosimeter  
design for Ir-192 brachytherapy

P.P.Cruijssen



# Master Thesis

Feasibility study for an in-vivo scintillator-fibre  
dosimeter design for Ir-192 brachytherapy

by

P.P. Cruijssen

To obtain the degree of Master of Science  
at the Delft University of Technology,  
to be defended publicly on Tuesday January 11, 2022 at 11:00 PM.

|                   |  |                            |
|-------------------|--|----------------------------|
| Student number:   | 4167236                                  |                            |
| Thesis committee: | Assistant professor dr. ir. A.G. Denkova | TU Delft, chair            |
|                   | Dr. ir. D. S. Dihalu                     | TU Delft, Daily supervisor |
|                   | Dr. ir. M. C. Goorden                    | TU Delft, supervisor       |
|                   | Drs. F. P. de Vries                      | Elekta, Daily supervisor   |

*This thesis is confidential and cannot be made public.*

An electronic version of this thesis is available at <http://repository.tudelft.nl/>.





# Abstract

High dose-rate (HDR) brachytherapy (BT) is radiation therapy (RT) which temporarily inserts a highly radioactive source into the planning target volume (PTV) with the use of an afterloader, applicator, transfer tubes, needles and planning software. The dose delivered to a point in the tumour depends on the type and activity of the source, the distance to the source and the time the source dwells at a predetermined dwell position. Current therapies have proven to be capable of tumour control. However, in contrast with other RTs there is no suitable integrated dose verification method available for HDR BT which does not disturb the clinical workflow. The focus of this research is on the dose verification for the most commonly used form of HDR BT. The one with the  $^{192}\text{Ir}$  source. An optical *in vivo* dosimetry (OIVD) sensor assembly consists of a capsuled scintillator coupled into an optical fibre, which connects to a photodiode capable of processing the light signal generated in the scintillator. These systems are currently only available in experimental set-ups and not yet integrated with the afterloader, making them clinically unusable. Furthermore, the system needs to be coupled with an optical fibre of 100-300 $\mu\text{m}$ , give a linear output signal to remodel the delivered dose, be non-hygroscopic, be suitable at treatment temperatures, and have low production costs.

By adding a OIVD sensor to the current clinical BT workflow, better treatment can be achieved. This sensor assembly needs to be made with a suitable scintillator and shape to have a high coupling efficiency in the OIVD sensor system to give reliable dose verification. Both a literature study and simulations are executed as part of my master thesis to provide a context for the project and to find the best-suited shape and scintillator. This report provides an overview of the current status of knowledge of OIVD from the available experiments and clinical studies derived from the published data, so knowledge for choosing the scintillator material, fibre diameter and the coupling geometry can be obtained. Special attention is given to identifying why scintillators excite light of a specific wavelength and how to achieve an efficient light coupling.

The inorganic scintillator  $\text{ZnSe} : \text{O}$  has favourable scintillation characteristics and is has proven itself to be helpful in a OIVD sensor for  $^{192}\text{Ir}$  BT with its high intensity, good energy resolution, slight afterglow and low production cost. The experimental part of this research is the verification of the OIVD sensor assembly with simulations executed within the COMSOL Multiphysics® ray-tracing package, which compares multiple similar OIVD sensor assembly heads. The OIVD model is inspired by the experimental set-up from E.Andersen and simulates for multiple configurations on a range of parameters (5).

The simulations of the OIVD sensor assembly can conclude the following:

1. The most favourable scintillator is  $\text{ZnSe} : \text{O}$ , this scintillator has the highest light yield and low absorption.
2. With a fibre diameter of 200 $\mu\text{m}$ , sufficient light yield reaches the detector to verify the dose delivery.
3. Couple the fibres off the centre from the central axis of the scintillator will negatively influence the coupling efficiency.

The outcome of this research contributes to the design of a OIVD sensor assembly for HDR BT for with  $^{192}\text{Ir}$ . These simulations lead to an optimal design that will fit the current afterloader system. Next to this, the OIVD sensor assembly head can be made with simple manufacturing steps so that it can be produced at a minimal cost. The combination of the COMSOL model with the scintillation properties from the literature shows that a sensor assembly of a ball coupled  $\text{ZnSe} : \text{O}$  scintillation is has a higher light throughput than the prototype from E.Andersen (5), this shows that it is favourable to verify the dose delivery of  $^{192}\text{Ir}$  HDR BT (5).



# Preface

Before you lies the thesis which completes my Biomedical engineering master. Completing this thesis would not be possible without the help from the following people, in these strange times while working from home (in no particular order),

1. Dosti Dihalu, my TU Delft supervisor, after sparking my interest in radiation safety and measurement in one of his lectures, he was open to discussing the possibility of supervising my master thesis and guiding me during the ups and downs of this thesis.
2. Frits de Vries, my Elekta supervisor, who initiated this master research. His expertise in brachytherapy (BT) and *in vivo* dosimetry (IVD) provided valuable input, and he made it possible for me to jump aboard this research project.
3. Antonia Denkova, the very personal treatment and assignment definition have committed me to the work that I needed to do

I would also like to thank all my fellow students from the master specialisation in medical physics, who made the first part of my master unforgettable. Finally, I could not have done this without my family and friends, particularly Nina. They have unconditionally supported me and encouraged me to take this opportunity, as well as many opportunities during my studies and years in Delft.

*Pepik Petrus Cruijssen*  
*Rotterdam, January 2022*





# Contents

|   |      |
|---|------|
| Abstract  | iii  |
| Preface   | v    |
| List of tables  | ix   |
| List of figures   | xi   |
| List of abbreviations   | xiii |
| List of symbols   | xv   |
| 1 Introduction  | 1    |
| 1.1 Objective and research questions.   | 2    |
| 1.2 Structuring.  | 3    |
| 2 Background  | 5    |
| 2.1 Brachytherapy   | 5    |
| 2.2 Current status of brachytherapy   | 5    |
| 2.3 Dose calculation for brachytherapy  | 6    |
| 2.4 Fibre-coupled dosimeters used in brachytherapy  | 6    |
| 2.5 Challenges for in-vivo dosimetry for brachytherapy  | 6    |
| 3 Literature research: Luminescence dosimetry   | 9    |
| 3.1 Physical mechanism of scintillation   | 9    |
| 3.2 Interactions of ionising radiation with the scintillators   | 9    |
| 3.2.1 Photoelectric effect.   | 10   |
| 3.2.2 Compton scattering  | 11   |
| 3.2.3 Pair Production   | 12   |
| 3.3 Ionization  | 13   |
| 3.4 Relaxation of electrons and holes.  | 14   |
| 3.5 Excitation and Emission of luminescence centres   | 14   |
| 3.6 General requirements of scintillators   | 15   |
| 3.6.1 Light yield   | 15   |
| 3.6.2 Duration of the scintillation pulse   | 16   |
| 3.6.3 Optical properties  | 16   |
| 3.6.4 Energy resolution   | 16   |
| 3.6.5 Mechanical properties of the scintillator   | 16   |
| 3.6.6 Stem Effect.  | 16   |
| 3.6.7 Cost considerations   | 17   |
| 3.7 Selection of suitable scintillator material for the tip of an optical in-vivo dosimetry sensor assembly | 17   |
| 3.7.1 Current scintillators used for HDR brachytherapy IVD?   | 17   |
| 4 Literature research: Optical Transmission   | 19   |
| 4.1 Structure of optical fibre  | 19   |
| 4.2 Propagation of light  | 20   |
| 4.2.1 Attenuation of light  | 20   |
| 4.2.2 Reflection of light   | 20   |
| 4.2.3 Refraction of light   | 20   |
| 4.2.4 Light transmission  | 20   |

|       |  |    |
|-------|--|----|
| 4.3   | Fibre coupling efficiency . . . . .  | 21 |
| 4.4   | Acceptance angle of an optical fibre . . . . .                                       | 21 |
| 4.5   | Signal To Noise. . . . .   | 22 |
| 5     | Method . . . . .   | 23 |
| 5.1   | Design outline and justifications . . . . .  | 23 |
| 5.2   | Physics of the model . . . . .   | 23 |
| 5.2.1 | Ray optics . . . . .   | 24 |
| 5.2.2 | Wave optics . . . . .  | 24 |
| 5.3   | Parameter identifications. . . . .   | 24 |
| 5.3.1 | Operational parameters . . . . .   | 24 |
| 5.3.2 | Scintillator parameters . . . . .  | 24 |
| 5.3.3 | Coupling parameters. . . . .   | 26 |
| 5.4   | Modelling work flow . . . . .  | 26 |
| 5.5   | literature background for the design . . . . .                                       | 27 |
| 6     | Simulations . . . . .  | 29 |
| 6.1   | Model verification . . . . .   | 29 |
| 6.1.1 | Refractive index and attenuation coefficient of the suitable scintillators . . . . . | 30 |
| 6.1.2 | Reflective coating . . . . .   | 30 |
| 6.1.3 | Finite Element method . . . . .  | 31 |
| 6.1.4 | Coupling efficiency of the fibre. . . . .  | 31 |
| 6.2   | Configuration of the OIVD sensor assembly . . . . .                                  | 32 |
| 7     | Results . . . . .  | 35 |
| 7.1   | Design overview . . . . .  | 35 |
| 7.2   | Light transmission in the COMSOL Multiphysics models. . . . .                        | 36 |
| 7.2.1 | Luminescence in COMSOL Multiphysics . . . . .  | 36 |
| 7.2.2 | Positioning of the optical fibre . . . . .   | 37 |
| 7.2.3 | Coupling between the scintillator and the optical fibre . . . . .                    | 37 |
| 7.3   | Comparison of the COMSOL OIVD models. . . . .  | 39 |
| 8     | Discussion . . . . .   | 41 |
| 8.0.1 | Optical validation of the COMSOL model . . . . .                                     | 41 |
| 8.0.2 | Validation of the current literature . . . . .                                       | 43 |
| 9     | Conclusion . . . . .   | 45 |
| 10    | Recommendations . . . . .  | 47 |
| 10.1  | Improvements of the COMSOL model . . . . .   | 47 |
| 10.2  | Fabrication of the OIVD sensor system. . . . .                                       | 48 |
| 10.3  | in-vitro and in-vivo testing of the OIVD model . . . . .                             | 49 |
|       | Bibliography . . . . .   | 51 |
| A     | Tables . . . . .   | 57 |
| B     | Remaining results . . . . .  | 59 |
| C     | COMSOL simulations . . . . .   | 65 |
| D     | MATLAB Scripts . . . . .   | 69 |
| D.1   | Parameter sweep analysis . . . . .   | 69 |
| D.2   | Seed points for the scintillator . . . . .   | 70 |

# List of tables

|     |   |    |
|-----|---|----|
| 3.1 | Summary of the most important characteristics of scintillation detectors. These are rated as beneficial (++) , good (+) , mediocre (+/-) and inconvenient (-) for high dose-rate (HDR) brachytherapy (BT) . . . . . | 18 |
| 5.1 | Design specification of eight optical <i>in vivo</i> dosimetry (OIVD) sensor assemblies . . . . .   | 27 |
| 6.1 | Refractive indices and absorption coefficients of multiple materials, COMSOL Multiphysics (CM) stands for the build-in material in COMSOL Multiphysics . . . . .  | 30 |
| 6.2 | Refractive indices of coating materials . . . . .   | 30 |
| 6.3 | The number of rays and the light intensity entering the optical fibre compared with the cable diameter. The initial number of rays released in the scintillator is 17640. . . . .                                   | 32 |
| 7.1 | Design overview of the COMSOL models . . . . .  | 35 |
| 7.2 | Light coupling efficiency . . . . .   | 39 |
| 7.3 | light coupling in the COMSOL models . . . . .   | 39 |
| 8.1 | Validation of the optical performance . . . . .   | 42 |
| A.1 | Physical characteristics of the scintillators . . . . .   | 58 |



# List of figures

|     |   |    |
|-----|---|----|
| 1.1 | The workflow when a patient receives radiation therapy. . . . .   | 1  |
| 1.2 | Diagrammatic view of the different components involved while using <i>in vivo</i> dosimetry (IVD) during brachytherapy (BT): 1. Needles 2. Template 3. Dwell position 4. stainless steel cable 5. Active Ir <sup>192</sup> source 6. Optical fibre 7. Scintillation Crystal 8. planning target volume (PTV) . . . . | 2  |
| 2.1 | Schematic desing and dimensions of Elekta's <sup>192</sup> Ir Flexisource®(86) (a) and provisional design or the optical <i>in vivo</i> dosimetry (OIVD) sensor tip (b). Dimensions are given in mm. . . . .  | 6  |
| 3.1 | The curtain graph demonstrates the regions in which each type of photon interaction dominates as a function of photon energy and atomic number Z of a material. where $\tau$ is the probability of the photoelectric effect, $\sigma$ of Compton scattering and $\kappa$ for pair production. . . . .               | 10 |
| 3.2 | Diagram illustrating the photoelectric effect: Complete transfer of photon energy to a bound atomic electron . . . . .  | 11 |
| 3.3 | Diagram illustrating the Compton effect: Transfer of a part of the photon energy to a weakly bound electron . . . . .   | 12 |
| 3.4 | Diagram illustrating pair production: Conversion of photon into an electron-positron pair in a strong coulomb field around high Z nucleus . . . . .   | 12 |
| 3.5 | Sketch of an ionization track formed by a primary electron (48): 1. The ionisation track of the primary electron 2. The created free holes 3. The created free electrons 4. Diffusion track of the created electrons and holes 5. Volume of a scintillation crystal . . . . .                                       | 13 |
| 3.6 | Schematic representation of the scintillation mechanism (4): A. Interactions B. Trapping of electrons C. Recombination D. Excitation. 1. Electrons 2. Holes 3. Energy level of the trapped electron 4.Excited photon . . . . .  | 14 |
| 3.7 | <sup>57</sup> Co pulse-height spectrum of Yttrium Aluminum Garnet doped with Cerium Y <sub>3</sub> Al <sub>5</sub> O <sub>12</sub> : Ce [1x1x0.7mm] (67) . . . . .  | 15 |
| 3.8 | (a) Emission spectra induced by an <sup>192</sup> Ir BT source of the 5 inorganic scintillators used in this study. (b)-(f) Inorganic scinillation detectors used in this study. (47, 10) . . . . .   | 17 |
| 4.1 | Structure of an basic optical fibre . . . . .   | 19 |
| 4.2 | An incoming light ray at the maximum acceptance angle enters and propagates through a step index fibre . . . . .  | 19 |
| 4.3 | (a) Refraction and reflection at the boundary between two media with different refractive indices, (b) critical angle and (c) total internal reflection (10) . . . . .  | 21 |
| 4.4 | An optical fibre coupled to a cylindrical scintillator. An annulus with thickness dz used in equation (4.7) is shown at the distance z from the fibre . . . . .   | 22 |
| 4.5 | a) Acceptance cone of a butt coupled fibre. (b) The lens added results in a chance in the numerical apertures (NA) and magnification of the fibre. (c) The equivalent of the lens added to the system, resulting in a wider optical fibre with a reduced NA(25) . . . . .   | 22 |
| 5.1 | The proposed outline in 2D and 3D of the OIVD sensor system design without background fibres  | 23 |
| 5.2 | Coupling geometries of two selected simulations, the pink colour represents the scintillator, the orange the optical adhesive and the cyan the fibre core . . . . .   | 26 |
| 6.1 | The behaviour of an incoming light ray at the material transition from scintillator to fibre without attenuation, both executed in the ray- and wave-optics module in COMSOL Multiphysics .   | 29 |
| 6.2 | Reflectance of zirconium Oxide layer between a ruby and the stainless steel capsule when a light ray hits the stainless steel capsule perpendicular . . . . .   | 31 |
| 6.3 | A dedicated mesh size for the individual domains . . . . .  | 31 |
| 6.4 | The coupling efficiency of the model presented by E.Andersen (5) as a function of the diameter of the optical fibre . . . . .   | 32 |

|     |  |    |
|-----|--|----|
| 6.5 | The COMSOL model with capsule and $Al_2O_3$ scintillator . . . . .   | 33 |
| 6.6 | The model with capsule compared with the model described by E.Andersen . . . . .   | 33 |
| 7.1 | Design overview of the COMSOL models to investigate the coupling efficiency . . . . .  | 36 |
| 7.2 | The behaviour of an incoming light ray at the material transition from scintillator to fibre without attenuation, executed in the ray-optics module in COMSOL Multiphysics . . . . . | 36 |
| 7.3 | OIVD model inspired by E. Andersen . . . . .   | 37 |
| 7.4 | Light coupling efficiency at the entrance of the PMMA fibre . . . . .  | 38 |
| 7.5 | The attenuation of $\lambda = 610nm$ light in a $Al_2O_3 : C$ scintillator. With an adjusted 28 vertical grid points in the y-direction instead of 7. . . . .                        | 38 |
| A.1 | Periodic Table of the Elements with the Lanthanides highlighted . . . . .  | 57 |
| B.1 | Handboek Radionucliden, A.S. Keveling Buisman Ir-192 (page 214) . . . . .  | 60 |
| B.2 | Handboek Radionucliden, A.S. Keveling Buisman Ir-192 (page 215) . . . . .  | 61 |
| B.3 | The behaviour of an incoming light ray at the material transition from scintillator to fibre without attenuation, executed in the ray-optics module in COMSOL Multiphysics . . . . . | 62 |
| B.4 | The behaviour of an incoming light ray at the material transition from scintillator to fibre without attenuation, executed in the ray-optics module in COMSOL Multiphysics . . . . . | 63 |
| C.1 | The COMSOL steps taken for the encapsulated OIVD sensor assembly with the $ZnSe : O$ scintillator and the silica-doped fibre by CeramOptec. . . . .                                  | 67 |

# List of abbreviations

| <b>Notation</b> | <b>Description</b>                                |
|-----------------|---|
| BED             | biologically effective dose                       |
| BT              | brachytherapy                                     |
| CB              | conduction band                                   |
| CM              | COMSOL Multiphysics                               |
| CT              | computed tomography                               |
| e-h             | electron-hole                                     |
| EBRT            | external beam radiation therapy                   |
| EU              | European Union                                    |
| FEM             | Finite Element Method                             |
| FWHM            | full width at half maximum                        |
| GOP             | geometrical Optics                                |
| GTV             | gross tumor volume                                |
| HDR             | high dose-rate                                    |
| ISD             | inorganic scintillator detector                   |
| IVD             | <i>in vivo</i> dosimetry                          |
| LDR             | low dose-rate                                     |
| LINAC           | linear accelerator                                |
| MOSFET          | metal oxide semiconductor field effect transistor |
| MR              | magnetic resonance                                |
| MRI             | magnetic resonance imaging                        |
| NA              | numerical apertures                               |
| NOA61           | Norland Optical Adhesive                          |
| OAR             | organ at risk                                     |
| OIVD            | optical <i>in vivo</i> dosimetry                  |
| PE              | primary electron                                  |
| PTV             | planning target volume                            |
| RH              | ray heating                                       |
| RL              | radioluminescence                                 |
| RT              | radiation therapy                                 |
| S/N             | signal to noise                                   |
| TG-43           | task group No. 43                                 |
| TIR             | total internal reflection                         |
| TLD             | thermoluminescent dosimeter                       |
| VB              | valance band                                      |





# List of symbols

## Mathematical notation

$\odot$  element-wise multiplication

## Greek symbols

|               |  |                               |
|---------------|--|-------------------------------|
| $\beta$       | Numerical coefficient for band gap compounds $\beta = 1.5 - 3$                     | -                             |
| $\gamma$      | Penetrating form of electromagnetic radiation                                      | -                             |
| $\kappa$      | The imaginary part of the refractive index   | $m^{-1}$                      |
| $\lambda$     | The wavelength $\lambda$ of a sinusoidal waveform travelling at constant speed $v$ | m                             |
| $\Lambda$     | Kerma-rate constant  | $Gy \cdot m^2 Bq^{-1} h^{-1}$ |
| $\sigma_{pe}$ | probability of the photoelectric effect  | -                             |
| $\sigma_{ce}$ | probability of the compton scattering  | -                             |
| $\sigma_{pp}$ | pronability of the pair production   | -                             |

## Latin symbols

|             |  |                      |
|-------------|--|----------------------|
| $A$         | The absorbance of light  | -                    |
| $c$         | Speed of light in a vacuum inertial system $c = 299.792458 \cdot 10^6$ | $m \cdot s^{-1}$     |
| $\dot{D}$   | The absorbed dose rate   | $mGy \cdot sec^{-1}$ |
| $E_b$       | Binding energy of electron   | eV                   |
| $E_e$       | Energy of an electron  | eV                   |
| $E_g$       | Bandgap energy   | eV                   |
| $E_{ke}$    | Kinetic energy   | eV                   |
| $E_\gamma$  | Photon energy  | eV                   |
| $E'_\gamma$ | Energy of an Compton scattering photo electron                         | eV                   |
| $Gy$        | Gray - derived unit of ionizing radiation                              | Gy                   |
| $h$         | Planck constant $h = 6.62607015 \cdot 10^{-34}$                        | J·s                  |
| $I$         | Intensity of a photon  | $W \cdot m^{-2}$     |
| $\dot{K}$   | Kerma  | Gy                   |
| $m_e$       | Mass of a free electron $m_e = 9.10938356 \cdot 10^{-31}$              | kg                   |
| $n$         | The ratio between the speed of light in vacuum and a medium            | -                    |
| $Q$         | Luminescence quantum efficiency  | -                    |
| $S$         | Electron-hole transfer efficiency to the luminescence center           | -                    |
| $S_{sh}$    | shielding constant   | -                    |
| $T$         | Transmittance of light   | -                    |
| $v_m$       | Speed of light in a medium   | $m \cdot s^{-1}$     |
| $Z$         | Atomic number  | -                    |
| $Z_{eff}$   | effective nuclear charge $Z_{eff} = Z - S_{sh}$                        | -                    |



# 1

## Introduction

Cancer is one of the leading causes of death worldwide. In 2019, a total of 1,410,000 cancer deaths were estimated in the European Union (EU) alone (54). Cancer treatment primarily consists of three clinical treatment modalities: Radiation therapy (RT), surgery and chemotherapy. A combination is chosen according to the size, stage, type of tumour, patient condition, and personal preferences. To maintain a high quality of life during and after treatment. RT has a long history which started after the discovery of  $^{226}\text{Ra}$  by Marie and Pierre Curie in 1898. RT can be categorized into three main groups: External beam radiation therapy (EBRT), systemic radioisotope therapy and brachytherapy (BT).

The first clinical results on BT in cervical cancer surpassed the results obtained through conventional methods in 1913 (1, 72). Since then, several developments have improved the effectiveness, conformality and homogeneity of dose distributions and radiation exposure to personnel. In the following years,  $^{226}\text{Ra}$  was replaced by artificially created radionuclides such as  $^{137}\text{Ce}$ ,  $^{60}\text{Co}$  and  $^{192}\text{Ir}$  (37). Nowadays, BT can be provided using high dose-rate (HDR) or low dose-rate (LDR), depending on the source type and length of time the radioactive source remains at a certain position. This research focuses on HDR BT, where a highly radioactive source is temporarily inserted with the help of thin transfer tubes and needles, in the planning target volume (PTV). One of the main challenges of HDR BT is to position the source at the predetermined location. To achieve this, an applicator, thin transfer tubes, or both can be used. The needles are placed into the predetermined position during surgery, and the  $^{192}\text{Ir}$  source is loaded at the dwell position during the RT. These dwell positions are determined during the dosimetric study where 95% of the PTV gets 100% of the prescription dose during treatment (92). This dose delivery is planned using computed tomography (CT) images, where accurate initial localisation of the patient anatomy and implanted transfer tubes are visualised. Ideally, the insertion of the transfer tubes and applicator, the treatment planning, and treatment delivery is performed over a short time without moving the patient. The loading of the source can be done manually or with a remote-controlled afterloader. The advantages of the afterloader are that there is no dose delivery to the personnel. Besides that, it also improves the conformality and the quality of the dose distribution.



Figure 1.1: The workflow when a patient receives radiation therapy.

According to Public Health England, 1.0% of the registered radiotherapy errors are a result of mistakes made during BT treatment (26). Treatment errors in BT are divided into two groups: human errors and malfunctions of the equipment. Where human error is the prime cause of radiation errors, within this group, the most reported error is the misplaced initial position of the applicator (26). Additionally, treatment delivery verification is less advanced in BT than EBRT due to the local dose delivery and the limited space available.

To improve the current BT treatments, staff needs to get real-time insight in the delivered dose, with a maximum delay of 5 seconds (27). Real-time *in vivo* dosimetry (IVD) can provide efficient error treatment verification and detection. The latest research in RT shows that tumour treatments can be improved when patients receive a focal boost to the residual Gross tumor volume (GTV) with BT after EBRT (82). To measure the real-time *in vivo* delivered dose in the available transfer tubes the dosimeter needs to be restricted by the

volume constraints of 0.7mm x 3.5 mm. The magnetic resonance (MR)-linear accelerator (LINAC), is setting a new standard for EBRT. However, the magnetic field used in medical imaging brings extra challenges to the development of an IVD dosimeter.

Currently, there are three dosimeter types available that meet the dimension requirements: The thermoluminescent dosimeter (TLD), the semiconductor dosimetry systems such as the metal oxide semiconductor field effect transistors (MOSFETs) and silicon diodes and the scintillation dosimeters. Where only the MOSFET and the scintillation dosimeter have a detection efficiency suitable for IVD. To use the dosimeter in a treatment where BT is combined with the MR-LINAC it needs to withstand the magnetic field. The scintillation dosimeter can be made with materials that are not sensitive to magnetism and is therefore most suitable (17).

In this report, a study is presented to find the best suitable scintillator and the most efficient coupling for the head of an optical dosimeter. This sensing part has four constraints:

1. The sensing part needs to fit in the currently available transfer tubes and is therefore limited by a cylindrical shape with a length of 3.5mm and a diameter of 0.7mm, see figure 2.1b.
2. The scintillation crystal needs to detect the emitted  $\gamma$ -rays of the  $^{192}\text{Ir}$  isotope.
3. The scintillation light need to be coupled into an optical fibre with a diameter of 100-300 $\mu\text{m}$ .
4. The sensor tip needs to be non-hygroscopic and resistant to the temperature during BT application.

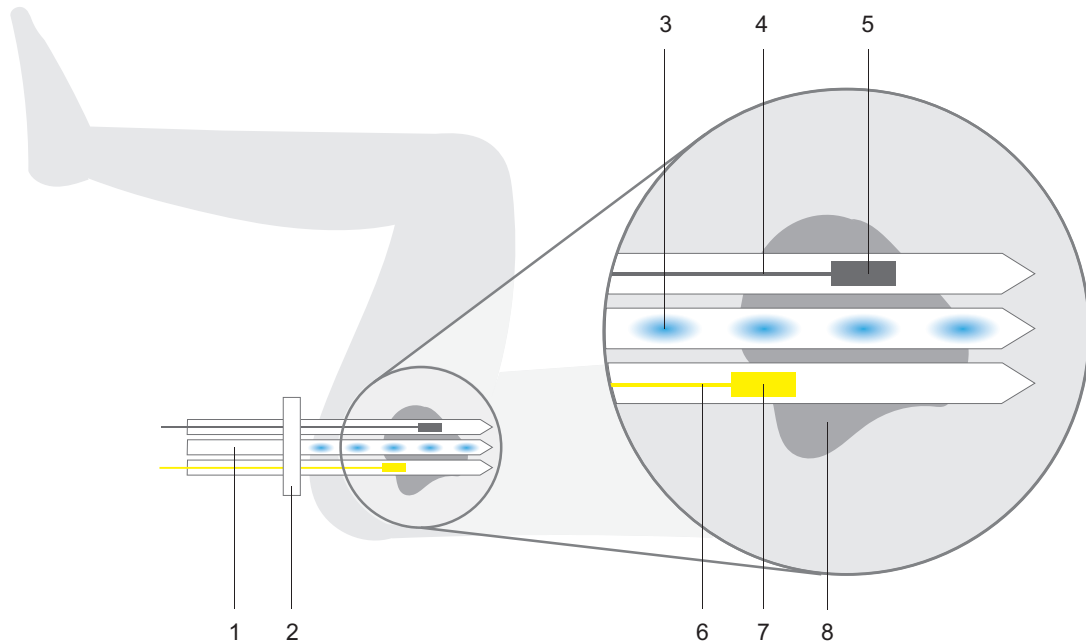


Figure 1.2: Diagrammatic view of the different components involved while using IVD during BT:  
1. Needles 2. Template 3. Dwell position 4. stainless steel cable 5. Active  $\text{Ir}^{192}$  source 6. Optical fibre 7. Scintillation Crystal 8. PTV

## 1.1. Objective and research questions

The objective of this research is to provide an overview of the current state of the art for optical *in vivo* dosimetry (OIVD) sensor assembly and advice the company Elekta on the composition of the head of the assembly, given the needs as mentioned earlier. This is done by a literature study and by verifying the findings in simulation software carried out within the COMSOL Multiphysics® software package. The head of the IVD sensor assembly can be split into two parts: The scintillator and the optical coupling. Understanding the scintillation processes and the factors influencing these processes is critical in choosing the suitable scintillator for the limited volume available in the head of the IVD sensor assembly. Next to this, the behaviour of light in the sensor assembly is needed to couple the scintillation light efficiently into an optical fibre with a 100 $\mu\text{m}$  core, see figure 2.1b.

To fulfil this objective, the main research question must be answered:

**What are the smallest fibre diameter and simplest embodiment of an OIVD sensor assembly coupling to be able to obtain sufficient light yield, given the HDR brachytherapy application, the selected fibre, the available scintillator volume and scintillation materials?**

To achieve this, the following four sub-questions need to be answered:

1. How to maximise the number of ejected detectable photons in a scintillator irradiated by an  $^{192}\text{Ir}$  source to achieve sufficient light yield for the application?
2. What is the most suitable non-hygroscopic scintillator that fits in the head of an IVD sensor assembly?
3. How to maximise the light coupling efficiency by adjusting the shape of the scintillator, given the maximum dimension of the IVD sensor assembly?
4. What is the minimum thickness of the optical fibre while maintaining sufficient light yield for the application?

## 1.2. Structuring

These research questions are answered throughout this thesis, according to the following structure:

- Chapter 2 will discuss the current state of the art by first giving an introduction to BT and its relevance. This is followed by a section of the current error made during these therapies. Next, the challenges for the sensing part of an IVD assembly are covered. Finally, different dosimeters used for BT are discussed, together with the choices made on which dosimeters to use for this report.
- Chapter 3 covers the physical mechanism of scintillation, as well as the characteristic properties of scintillators. In addition, the currently available scintillators are compared.
- Chapter 4 states the requirements for the fibre coupling in the OIVD sensor assembly. This is followed by multiple mathematical methods to get insight into the coupling efficiency.
- Chapter 5 states the requirements for the OIVD system to implement it in COMSOL Multiphysics (CM) and the optical parameters in the fibre coupling subsystem.
- Chapter 6 tests the different parts of the OIVD sensor assembly in CM.
- Chapter 7 shows the performance of the system.
- Chapter 8 marks the end of the study, where the results are discussed.
- Chapter 9 Finalises the report with the conclusion.
- Chapter 10 gives recommendations to improve the simulation model and to give possible directions for future research.



# 2

## Background

This chapter will discuss *in-vivo* dosimetry for brachytherapy (BT) and how it can improve the current clinical treatment for high dose-rate (HDR)-BT. The clinical use of BT and the benefits relative to external beam radiotherapy is discussed in Section 2.1. Secondly, the treatment delivery errors in brachytherapy are mentioned. Next, the challenges for *in vivo* dosimetry (IVD) are discussed. Finally, different kinds of IVD are introduced, which is concluded with the choices made for the dosimeter used for this research.

### 2.1. Brachytherapy

Brachytherapy is a type of radiation therapy that uses encapsulated radionuclide sources to treat tumours from a short distance. During the treatment, this radionuclide is placed near and into the planning target volume (PTV). This treatment allows a high dose to the unhealthy target volume while giving a lower dose to the surrounding healthy tissue. BT can be categorized in HDR and low dose-rate (LDR) which is based on the treatment dose rate, duration and implant type. Currently, BT is most used for the treatment of gynaecological, prostate, breast, head & neck and intraluminal tumours (89). HDR-BT is proven to be effective in the treatment of the tumours that need to receive a high biologically effective dose (BED) in the most conformal way (78). All the treatment plans for brachytherapy are performed using the task group No. 43 (TG-43) protocol (69). The most commonly used source for HDR-BT is  $^{192}\text{Ir}$ , this source has a half-life of 73.38 days, and average photon energy of 380 keV (15).

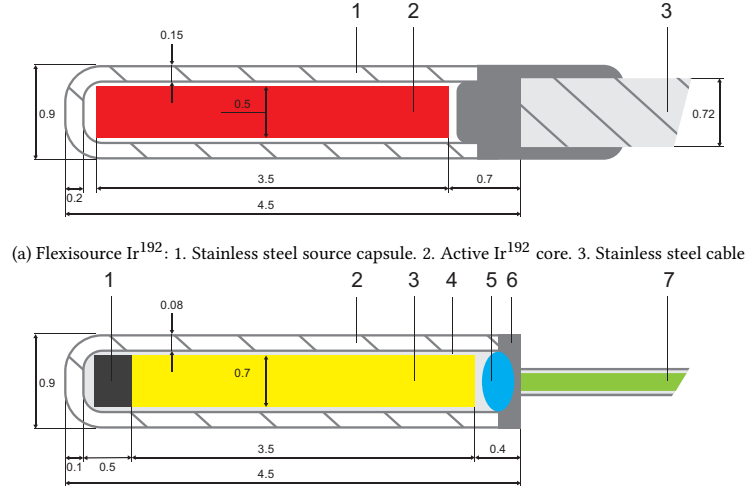
In some cases BT is combined with external beam radiation therapy (EBRT) which can result in better tumour control (79). Therefore multiple research groups study the results in combined HDR-BT with EBRT (19). The current results are promising and stimulate to combine the magnetic resonance (MR)-linear accelerator (LINAC) with BT equipment more often. To improve the results even further millimetre source tracking is highly desirable (41). Nonetheless, two of the current available source tracking systems, the metal oxide semiconductor field effect transistors (MOSFETs) and thermoluminescent dosimeters (TLDs)) are not suitable because of the magnetic field in the MR-LINAC. Therefore it is a requirement to get a luminescence dosimetry system which can operate when the magnetic resonance imaging (MRI) is in use.

### 2.2. Current status of brachytherapy

BT delivers a high conform dose of radiation to the PTV with sparing of the healthy surrounding organs at risk. However, some errors might still occur. The most common mistake in BT is the inadequate placement of the source, which occur because of bending and deflection of the needles. There are multiple reported errors for HDR-BT without the use of IVD-sensors (38, 84, 62).

Currently, multiple research groups report that through the use of a phantom and/or simulations of error scenarios, multiple of these errors could be detected with real-time IVD (6, 81, 45, 44).

When IVD gets implemented in the clinical workflow, in addition to image-guided BT, geometric information about the treatment progression is provided. With this, errors can be detected, which improves the quality of the therapy.



(a) Flexisource Ir<sup>192</sup>: 1. Stainless steel source capsule. 2. Active Ir<sup>192</sup> core. 3. Stainless steel cable

(b) Provisional design of the OIVD sensor tip: 1. reflector for reflectance measurement 2. Protective capsule. 3. Crystal scintillation material of 1.347 mm<sup>3</sup>. 4. Coating with a lower refractive index than the scintillation crystal. 5. Lens 6. Cable coupling 7. Optical fibre.

Figure 2.1: Schematic desing and dimensions of Elekta's <sup>192</sup>Ir Flexisource®(86) (a) and provisional design or the OIVD sensor tip (b). Dimensions are given in mm.

### 2.3. Dose calculation for brachytherapy

The TG-43 describes the absorbed dose calculations for BT treatments with <sup>192</sup>Ir. This report provides insight into the absorbed dose calculations by using water as a reference medium for the human tissue. With this, the absorbed dose rate can be calculated at the point of interest by using equation (2.1) (43).

$$\dot{D}(r, \theta) = \dot{K}_s \cdot \Lambda \cdot \frac{G_L(r, \theta)}{G_L(r_0, \theta_0)} \cdot g_L(r) \quad (2.1)$$

Where  $\dot{D}$  is the absorbed dose rate,  $r$  the distance between the centre of the <sup>192</sup>Ir source and the point of interest,  $\theta$  is the angle between the location of the source and the point of interest. Both  $r_0$  and  $\theta_0$  refer to the reference point ( $r_0 = 1\text{cm}$ ,  $\theta_0 = 90^\circ$ ).  $\dot{K}_s$  is the air-kerma rate of the source in vacuum at the reference distance.  $\Lambda$  is the Kerma-rate constant of the source and is related to the  $\dot{K}_s$ .  $G_L(r_0, \theta_0)$  is a geometrical function that describes the dose fall-off due to the inverse-square law and  $g_L(r)$  is the radial dose function which describes the dose fall-off due to photon scatter and attenuation.

### 2.4. Fibre-coupled dosimeters used in brachytherapy

IVD can provide real-time error detection and treatment verification during BT. Nonetheless, it is also known that implementations of these IVD sensor systems are hardly used by the clinical personnel. The current optical *in vivo* dosimetry (OIVD) sensor assemblies contain a detector that is coupled into an optical fibre. The detector proportionally emits light to the absorbed dose, as described in chapter 3. Furthermore, this light is coupled into the optical fibre. The 0.9 mm outer diameter of the dosimeter tip allows the sensory system to be used in the already available transfer tubes for dose delivery by the source, see figure 2.1b.

### 2.5. Challenges for in-vivo dosimetry for brachytherapy

A scintillation dosimeter has desirable characteristics for IVD in BT. Nevertheless, there are also difficulties. The major difficulties are the high dose gradients delivered by the source (2.1a). This requires an optical dosimeter with a small scintillation volume that ensures the flexibility of the dosimeter and the accuracy in measuring both high and low photon energies.

In addition, the current optical dosimeters produce a stem effect: Light induced by radiation of the fibre and the generated Cerenkov light. This undesirable light arises because the photon energy spectrum for the <sup>192</sup>Ir source is between 0.136-1.06 MeV (with an average energy of 380 keV), which is above the threshold energy for Cerenkov production in polymethyl methacrylate (PMMA), 178 keV. Therefore it is necessary to implement a removal technique, to improve the accuracy of the measurement (80).



For further development of OIVD sensor systems, it's important to have an accurate depth dose measurement. During the treatment, the dosimeter can be used at different distances of the  $^{192}\text{Ir}$  source and must therefore provide an accurate dose reading.

The OIVD detectors can be made without electrical components, which allows dosimetry measurements while the patient is in a MRI scanner.



# 3

## Literature research: Luminescence dosimetry

Since the use of the spintharoscope by Crookes in 1903, scintillators became essential for measuring ionising radiation (52). When scintillators are exposed to ionising radiation, a flash of light is emitted as a response. Scintillation can be observed in various inorganic and organic solids (56), fluids (30) and gasses (51). The understanding of the relationship between the energy deposited by the  $^{192}\text{Ir}$  source and the signal produced by the scintillator is essential to measure the delivered dose with a scintillator. This chapter describes the physical mechanism of scintillation. First, the interactions of a scintillator exposed to  $\gamma$ -radiation are described, followed by the effect of dopants on the properties of the scintillation crystal. Lastly, the characteristic properties of the fibre-coupled scintillators are presented.

### 3.1. Physical mechanism of scintillation

When ionising radiation hits a scintillator crystal, a flash of light is emitted. This phenomenon is called radio-luminescence (RL); before this phenomenon can be observed, a series of events happen in the scintillator. This can be described as a Five-step process (13, 91, 71): First the absorption of the  $\gamma$ -radiation and the electron-hole pair creation are described in section 3.2 and section 3.3. Followed by relaxation of the primary electrons in section 3.4. Thirdly the thermalisation of the low-energy secondary electrons occurs, resulting in electron-hole (e-h) pairs with corresponding bandgap energy. After this, the energy transfers from the e-h pairs to the luminescence centres. Finally, section 3.5 describes the luminescence centres emit photons in the visible light spectrum.

### 3.2. Interactions of ionising radiation with the scintillators

A scintillator absorbs ionising radiation and creates primary electrons and holes. This is the first stage in the scintillation process. When radiation hits a scintillating material, a part of the absorbed energy is transferred into a light flash. The wavelength and the number of photons measured in this light flash are dependent on the energy of the incoming particle (50). This study focuses on the interaction with  $\gamma$ -radiation. Therefore, only photon and electron interactions are elaborated. There are three ways how photons can interact with matter: Photoelectric effect, Compton scattering, and pair production (71). Since no photon-rays of the  $^{192}\text{Ir}$  exceed the 1022 keV, only little pair production will be detected. The interactions occurring in the scintillator produce a flash of light which can be measured with a photodetector; this phenomenon makes scintillators suitable for dosimetry.

The total absorption probability of an  $\gamma$ -ray by an electron  $\sigma_e$  can be calculated by solving equation (3.1) (71). Where  $\sigma_{pe}$ ,  $\sigma_{ce}$  and  $\sigma_{pp}$  denote the probability for the photoelectric effect, Compton scattering and pair, see figure 3.1. The ratio in which these effects take place in the scintillator depends on the energy on the incident photon  $E_\gamma$  and the atomic number  $Z$  (71).

$$\sigma_e = \sigma_{pe} + \sigma_{ce} + \sigma_{pp} \quad (3.1)$$

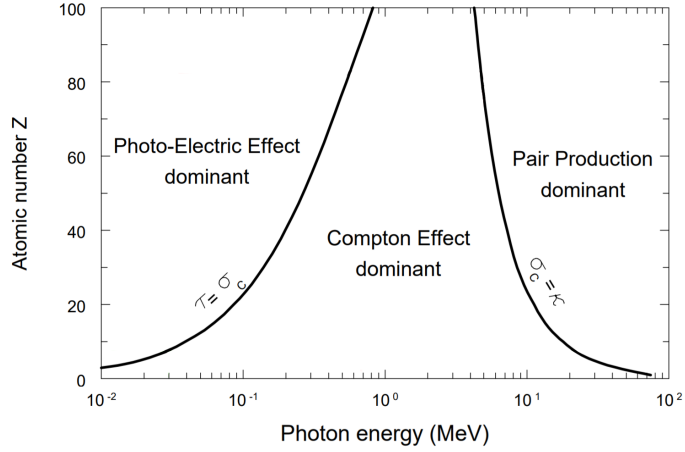


Figure 3.1: The curtain graph demonstrates the regions in which each type of photon interaction dominates as a function of photon energy and atomic number  $Z$  of a material. where  $\tau$  is the probability of the photoelectric effect,  $\sigma$  of Compton scattering and  $\kappa$  for pair production.

### 3.2.1. Photoelectric effect

The photoelectric effect is the emission of an electron when the incoming  $\gamma$ -radiation interacts with the scintillating matter. This occurs when an atom in the scintillator absorbs the incoming photon. The energy of the incoming photon can be determined with the Planck-Einstein relation 3.2 (33) where  $h$  denotes the Planck constant,  $c$  the speed of light in vacuum and  $\lambda$  the wavelength of the excited photon.

$$E_{\gamma} = \frac{h \cdot c}{\lambda} \quad (3.2)$$

The absorbed photon transfers all its energy, which results in the ejection of an electron (which is called a photoelectron) from the tightly bounded K- or L- shell (50). This electron obtains an energy  $E_e$  equal to the difference between the photon energy  $E_{\gamma}$  and the electron's binding energy  $E_b$ , described in equation (3.3) (71).

$$E_e = E_{\gamma} - E_b \quad (3.3)$$

This means that the photoelectric effect can only take place when  $E_{\gamma}$  is larger than  $E_b$  so a photoelectron can be ejected. The photoelectron leaves a track of holes and free electrons in the shells of the remaining atom. This leaves a vacancy in the K- or L- shell, which is filled by an electron from an energy shell further away from the atomic nucleus. The shift from a higher energy shell to a lower energy shell causes the emission of characteristic x-ray. Which in turn, transfers its energy to an outer-orbit electron which will be ejected from the atom and this electron is called an *Auger electron*. This is followed by a rearrangement of the remaining electrons of the atom (which is now an ion) (33, 68). The probability of the  $\sigma_{pe}$  decreases with the energy on the incoming photon  $E_{\gamma}$  and increases proportionally to the atomic number  $Z$  as in equation (3.4).

$$\sigma_{pe} \propto \frac{Z^n}{E_{\gamma}^{7/2}} \quad (3.4)$$

The exponential  $n$  varies between 4 and 5 depending on the photon energy (71). When observing figure 3.2, the photoelectric effect decreases with, and the number of interactions increases with a high atomic number.

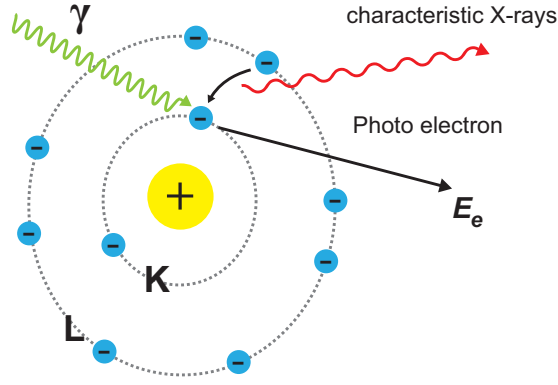


Figure 3.2: Diagram illustrating the photoelectric effect: Complete transfer of photon energy to a bound atomic electron

### 3.2.2. Compton scattering

Compton scattering is the ejection of an electron from its orbit after the collision between the incoming  $\gamma$ -particle and an electron. This takes place when the incoming photon interacts with a bound atomic electron and transfer part of the energy to this electron, which results in the excitation of a Compton scattering photon  $E'_\gamma$ , which has an energy described in equation (3.5) and a Compton electron.

$$E'_\gamma = \frac{E_\gamma}{1 + \frac{E_\gamma \cdot (1 - \cos(\theta))}{m_e \cdot c^2}} \quad (3.5)$$

Where  $m_e$  denotes the free electron mass and  $\theta$  the angle between the direction of the incoming photon and the scattered one, this scattered photon can leave the scintillator or can be absorbed in the crystal by photon interactions and will emit a light flash. The probability of absorption goes proportional to the scintillator size, so it will increase with the enlargement of the scintillator (71). When the scattered photon leaves the atom, the Compton electron will plough through the scintillation crystal and bring more atoms in the excited state. As observed in figure 3.1 the probability of Compton scattering occurs in most dominant in the region where the incoming photon has an energy between the 0.4-4 MeV. This can be determined with equation (3.6).

$$\sigma_c \propto \frac{Z}{E_\gamma} \quad (3.6)$$

All scattering angles will take place when using the scintillation dosimeter. Therefore a broad spectrum of energies can be exited. The highest deposited energy possible will occur when  $\theta$  in equation (3.5) is  $180^\circ$  (full back-scatter). It is impossible to transfer any more energy. Therefore, a sharp cutoff gives rise to the Compton edge (28).

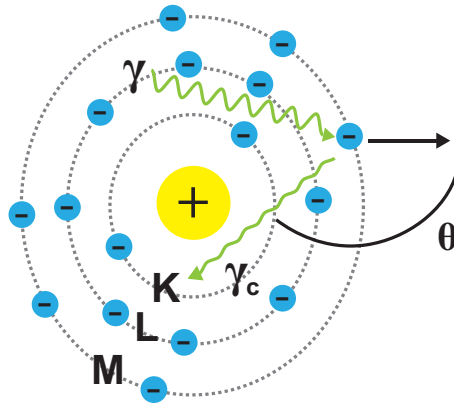


Figure 3.3: Diagram illustrating the Compton effect: Transfer of a part of the photon energy to a weakly bound electron

### 3.2.3. Pair Production

Pair production is the creation of an electron and positron. This occurs when an incident photon  $E_\gamma$  with an energy that exceeds 1022 KeV reaches the Coulomb field of the nucleus, see equation (3.7). As a reaction, an electron and a positron with  $E_{ke}$  are created. The energy of these particle can be calculated with equation (3.7) (76).

$$E_\gamma = 2 \cdot m_e \cdot c^2 + 2E_{ke} \quad (3.7)$$

The emitted positron will eventually annihilate with an electron, resulting in the emission of a photon with the energy of 511 keV. According to figure 3.4 the probability of the pair production increases proportionally with the increase of the energy of the incident photon and the atomic number  $Z$ .

$$\sigma_{pp} \propto Z^2 \cdot \ln(2) \cdot E_\gamma \quad (3.8)$$

When the incident photon has very high energy (5 GeV), the probability that pair production occurs reaches its maximum and will not increase further (71).

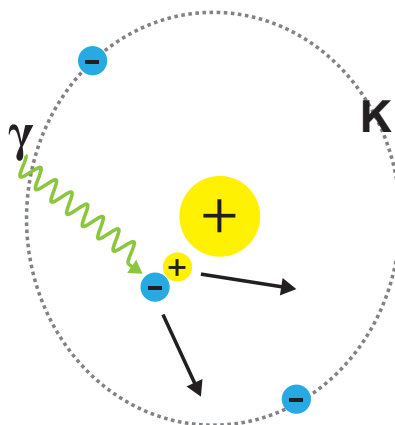


Figure 3.4: Diagram illustrating pair production: Conversion of photon into an electron-positron pair in a strong coulomb field around high  $Z$  nucleus

### 3.3. Ionization

The electrons generated from the  $\gamma$ -interaction due the photoelectric effect 3.2.1 , Compton effect 3.2.2 and pair production 3.2.3 are the primary electrons (PEs). These PEs undergo collision with other electrons while travelling through the scintillator. This results in energy loss by the excitation of secondary electrons and ionisation of the atoms close to the ionisation track of the incoming particle, see figure 3.5.

The number of collisions in the scintillator depends on the ionization density of the PE and  $\gamma$ -radiation. This can be quantified as the restricted linear collision stopping power ( $L_{\Delta}$ ) 3.9 (10). Which describes the average energy loss ( $dE$ ) due to the collisions of ionizing radiation traversing a distance ( $dl$ ).

$$L_{\Delta} = \left( \frac{dE}{dl} \right)_{\Delta} \quad (3.9)$$

All generated electrons will, on their turn, create new excitations where electrons move from the valence band to the conduction band (CB) see figure 3.6. This reaction will stop when all the energy of all electrons are too low to eject other electrons from its valence band. The result of this process is the creation of e-h pairs. The number of e-h-pairs increases proportionally to the energy of the PE (90). The number of e-h pairs  $N_{eg}$  can be calculated with equation (3.10), where  $\xi_{eh}$  is the average energy required to create a single e-h pair depending on the bandgap energy, and the type of material (71):

$$N_{eh} = \frac{E_{\gamma}}{\xi_{eh}} \quad (3.10)$$

Scintillation crystals suitable for *in vivo* dosimetry (IVD) need to recombine the excited electrons with the holes in the valance band (VB) via the emission of photons in the detectable spectrum. The number and energy of these photons is a measure for the incoming radiation by the  $^{192}\text{Ir}$  source. Therefore, the number of e-h pairs and the possibility that the electrons can reach the luminescence centres are essential for scintillation crystal.

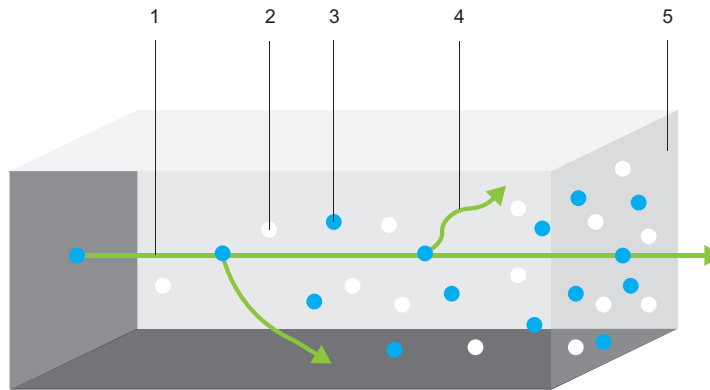


Figure 3.5: Sketch of an ionization track formed by a primary electron (48):

1. The ionisation track of the primary electron
2. The created free holes
3. The created free electrons
4. Diffusion track of the created electrons and holes
5. Volume of a scintillation crystal

### 3.4. Relaxation of electrons and holes

The next step in the scintillation process is the relaxation of the electrons and holes. This process starts when the energy of the electrons is below the ionisation threshold, which means that the energy of free electrons is too low to eject electrons from the VB of an electron. After this, the thermalisation stage starts. All the electrons will move to the bottom of the CB, and the holes move to the top of the VB, the leftover energy is released due to vibrations of the atoms (ions) in the network (63). Eventually, the energy between the electrons in the CB and the holes in the VB will be equal to the bandgap energy  $E_g$ , which brings the crystal to its thermal equilibrium. This phenomena makes scintillators temperature dependent.

Now the electrons and holes can move freely over the conduction and VB of the crystal scintillator. When these charge carriers meet a luminescence centre in the crystal, they get captured. The energy needed for the migration of the charge carries comes from both the electrostatic forces and the vibrations (58).

### 3.5. Excitation and Emission of luminescence centres

When a luminescence centre captures an electron, a migrating electron ( $e^-$ ) and hole (h) can recombine, and the luminescence centre will emit a light photon. A typical inorganic scintillator is an insulator with 4-12 eV gap between the top of the VB and the bottom of the CB, also known as the forbidden gap (4), see figure 3.6.

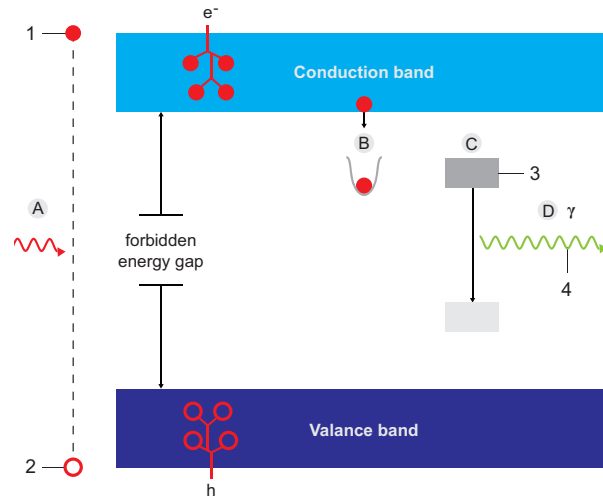
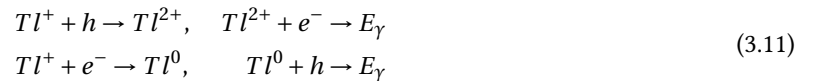


Figure 3.6: Schematic representation of the scintillation mechanism (4):  
 A. Interactions B. Trapping of electrons C. Recombination D. Excitation.  
 1. Electrons 2. Holes 3. Energy level of the trapped electron 4. Excited photon

As discussed in section 3.3, these PEs will undergo collision with other electrons while travelling through the scintillator, creating new electrons and holes. The recombination of these electrons in the CB and holes in the VB do not always recombine over the forbidden gap. In case of sodium iodide  $NaI$ , impurities of thallium ( $Tl^+$ ) are added to form the scintillation crystal  $NaI : Tl$  (71). The impurities are the so-called luminescent centres and have smaller bandgap energy than the forbidden gap. This allows more effective recombination of the electrons and holes. See figure 3.6.

For the crystal scintillators  $NaI : Tl$  it means that the luminescence center  $Tl^+$  is involved in the electronic recombination process (71):



The last process in the scintillation crystal is the emission of the luminescence centres where this scintillation pulse should have a high intensity and a short duration. Which is mainly determined by the luminescence dopant (22). Due to the different main electronic transitions in the scintillator, these dopants can be subdivided into different groups. For this research the mercury-like electronic transition from the  $^3P_1(sp) \rightarrow ^1S_0(s^2)$  orbital and the interconfigurational electronic transition from the  $5d \rightarrow 4f$  and the  $4f^65d \rightarrow 4f$  orbital are of interest (71).



Yttrium Aluminum Garnet doped with Cerium (YAG:Ce) is an example of a scintillation crystal that can recombine the holes and electrons efficiently at the luminescent centre due to the dopant, see figure 3.7. The recombination of the electrons and holes involves the  $5d \rightarrow 4f$  electronic transition (35). These luminescent centre  $Ce^{3+}$  in the lattice emit visible photons with a wavelength between 490-550nm. And therefore suitable as scintillation crystal for the optical *in vivo* dosimetry (OIVD) sensor assembly.

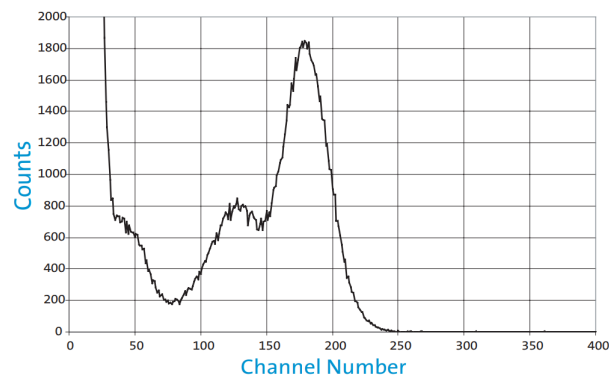


Figure 3.7:  $^{57}Co$  pulse-height spectrum of Yttrium Aluminum Garnet doped with Cerium  $Y_3Al_5O_{12} : Ce$  [1x1x0.7mm] (67)

### 3.6. General requirements of scintillators

To find a scintillation crystal suitable for IVD during brachytherapy (BT), it needs to meet the requirements describes in chapter 1. General important requirements for the performance of a scintillation crystal used in an OIVD sensor system are the following (4, 71):

1. Conversion efficiency and high scintillation light yield
2. Duration of the scintillation pulse
3. Optical properties
4. Energy resolution
5. Level of afterglow
6. Density of the material
7. Emission spectra
8. Non-hygroscopic material
9. Mechanical properties of the scintillator (hardness and ruggedness)
10. Possibility to manufacture the scintillation crystal
11. Cherenkov effect
12. Cost considerations

To my knowledge, no material meets all of these criteria. So the choice of a scintillator is always a compromise among these requirements. However, there are ways to improve the material properties by adding dopants. Scintillation crystals can be doped with elements that become a luminescence centre in the crystal because the bandgap energy is lower than the bandgap energy of the host. But there are also reasons to dope with elements that do not result in better light output but will improve other material properties (71). To use a scintillation crystal in a OIVD sensor assembly it must be robust. When the crystal cracks the light inside the crystal will scatter and therefore decrease the light yield and optical transmission of a scintillator. In this paragraph, the general scintillator mechanisms and properties are elaborated.

#### 3.6.1. Light yield

To make an effective OIVD sensor system, the scintillation crystals must have an effective conversion of ionising radiation to detectable light. This detectable light is the light yield and can be defined as the number of photons

exited from the scintillator per unit of absorbed energy. The maximum light yield ( $L_{max}$ ) of a scintillation crystal is limited by the electron-hole transfer efficiency to the luminescence centre ( $S$ ), the luminescence quantum efficiency ( $Q$ ), the coefficient for the bandgap compounds ( $\beta$ ) and the forbidden gap energy ( $E_g$ ) (70).

$$L_{max} = \frac{S \cdot Q}{\beta E_g} \times 10^6 \quad (3.12)$$

### 3.6.2. Duration of the scintillation pulse

The time response of a scintillation crystal mostly depends on the speed of the energy transfer in the luminescence centres (4). In most crystals, the intensity of the emission reaches their maximum at  $t=0$  (71). The  $5d \rightarrow 4f$  transition mentioned in section 3.4 contain the efficient dopants  $Ce^{3+}$ ,  $Pr^{3+}$ ,  $Nd^{3+}$ ,  $Tb^{3+}$  and  $Eu^{2+}$ . These all lanthanides which are shown in figure A.1. The decay time of these elements are all in the nanoseconds range (49).

### 3.6.3. Optical properties

The transmission and refraction of light are the two main optical characteristics of a scintillation crystal. When the light is emitted from the crystals luminescence centres, the crystal should transmit this light. The transmitted intensity of the light photons ( $I_x$ ) can be calculated with equation (4.1):

### 3.6.4. Energy resolution

The energy resolution of a scintillation crystals is the full width at half maximum (FWHM) intensity over the pulse-height spectrum, see figure 3.7 (71). The resolution ( $R_s$ ) of the scintillator is determined by multiple contributions and can be expressed as the quadratics sum of the transfer ( $R_t$ ), inhomogeneity ( $R_i$ ) and non-proportional resolution ( $R_n$ ) (71). See equation (3.13):

$$R_s^2 = R_t^2 + R_i^2 + R_n^2 \quad (3.13)$$

### 3.6.5. Mechanical properties of the scintillator

Most of the newly developed scintillation crystals are doped with other elements, which will emit the light photons in the visible spectrum as explained in section 3.5. Furthermore, the light yield of these scintillators with dopants will improve. However, some dopants decrease the light yield (71). These dopants are added to materials to make them more robust. This makes some scintillators more helpful to use in the OIVD sensor system.

### 3.6.6. Stem Effect

The stem effect that can be observed in the scintillator dosimetry system is caused by Cherenkov radiation and fluorescence light generated in the optical fibre of the detector when the system is exposed to the radiation field generated by the  $^{192}Ir$  source. Cherenkov radiation is electromagnetic radiation emitted when a charged particle (with energy greater than 175 keV) passes through a dielectric medium at a speed greater than the velocity of light in that medium. The amount of Cherenkov light produced in the cable and scintillator depends on the distance to the radioactive source. So when the source is close to the OIVD sensor tip and far from the fibre, the Cherenkov light is small compared to the desired scintillation light generated (31). Nonetheless, the length of the optical fibre is considerable. When the radiation field generated is constant, the generated Cherenkov light would be constant and could be accounted for in the calibration. Unfortunately, this would not happen during BT. The irradiation condition will depend on the distance to the source and the amount of fibre exposed to the radiation field that can vary from 2-40 cm. So the total amount of Cherenkov light can fluctuate between 5-50% (47).

For accurate dose delivery verification, a correction technique needs to be applied. This can be done with simple optical filtration techniques: where the violet-blue region of the visible spectrum is filtered out (80). Chromatic filtering (29), or background subtraction which makes use of multiple optical identical optical fibres that are placed parallel to each other, but only one optical fibre is attached to the scintillator and will carry the scintillation signal. However, an adverse effect of background subtraction is that it is more difficult to measure in case of high dose gradients. This is due to the rapid dose fall off due to the inverse square law. (10, 7).

### 3.6.7. Cost considerations

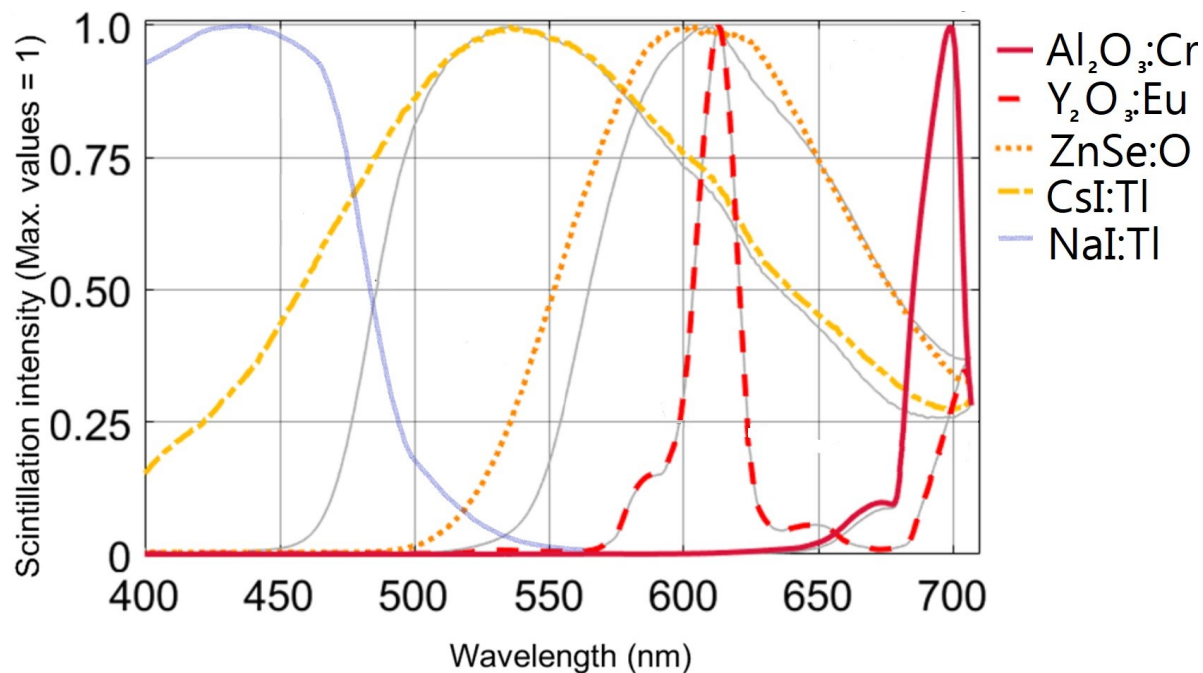
Low-cost materials and production techniques are desirable for manufacturing the OIVD sensor system. The required purity for the light yield performance, the availability of the crystal and the growth techniques are essential parameters for the cost of the scintillation crystal.

## 3.7. Selection of suitable scintillator material for the tip of an optical in-vivo dosimetry sensor assembly

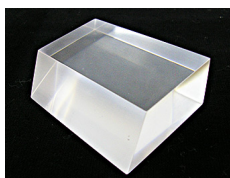
The scintillator in the OIVD sensor assembly fills the role of the detector. The most important properties for this are the scintillation efficiency, emission spectrum, decay time, attenuation coefficient, physical density, and the elemental composition (10).

### 3.7.1. Current scintillators used for high dose-rate (HDR) brachytherapy IVD?

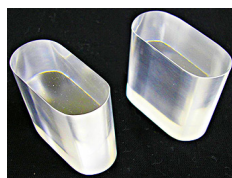
Various research groups tested OIVD sensor systems for HDR BT over the last five years (5, 74, 46). Most of the tested Inorganic scintillator detectors (ISDs) with a high atomic number are promising for real-time IVD. Currently,  $NaI : Tl$  is the detector of choice in multiple clinical measurement devices, and it is relatively inexpensive while having a high light output. Nevertheless, the energy resolution is poor, which limits the performance in application (21). The most promising widely available scintillators for IVD are  $Al_2O_3 : Cr$  (Ruby),  $Y_2O_3 : Eu$ ,  $ZnSe : O$  and  $CsI : Tl$ , see figure 3.8. These materials meet the earlier requirements when experimenting without the OIVD sensor assembly. But their investigation in such an assembly is desired. A summary of the characteristics of these ISDs are presented in section 3.7.1. Furthermore, more important properties of these and other scintillators can be found in appendix A.



(a) Emission spectra induced by an  $^{192}Ir$  BT source



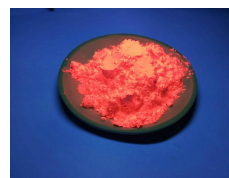
(b)  $NaI : Tl$



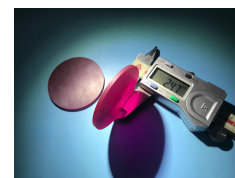
(c)  $CsI : Tl$



(d)  $ZnSe : O$



(e)  $Y_2O_3 : Eu$



(f)  $Al_2O_3 : Cr$

Figure 3.8: (a) Emission spectra induced by an  $^{192}Ir$  BT source of the 5 inorganic scintillators used in this study. (b)-(f) Inorganic scintillation detectors used in this study. (47, 10)

| Inorganic Scintillator                | Scintillation intensity | Little stem signal | Afterglow | Peak Emission | Cost | Ref.     |
|---------------------------------------|-------------------------|--------------------|-----------|---------------|------|----------|
| <i>NaI:Tl</i>                         | +                       | ++                 | +         | +             | ++   | (36)     |
| <i>Al<sub>2</sub>O<sub>3</sub>:Cr</i> | +/-                     | +                  | +         | +             | ++   | (46)     |
| <i>Y<sub>2</sub>O<sub>3</sub>:Eu</i>  | ++                      | +                  | -         | ++            | +    | (74)     |
| <i>ZnSe:O</i>                         | ++                      | ++                 | ++        | ++            | ++   | (20, 46) |
| <i>CsI:Tl</i>                         | +                       | ++                 | +/-       | ++            | +/-  | (88, 46) |

Table 3.1: Summary of the most important characteristics of scintillation detectors. These are rated as beneficial (++), good (+), mediocre (+/-) and inconvenient (-) for HDR BT

These inorganic scintillators have a high sensitivity per volume of material. In addition, they have longer luminescence lifetimes that improve the capabilities for stem signal removal, this makes them more suitable for OIVD sensor assemblies compared to the organic scintillators.

# 4

## Literature research: Optical Transmission

The geometry, material, and position must all influence the coupling efficiency in the optical *in vivo* dosimetry (OIVD) sensor assembly. This chapter will discuss the optical link between the scintillation crystal and optical fibre to the light measuring device. After the  $\gamma$ -radiation interacts with the scintillating material, the scintillation light emits. The aim is to couple this light efficiently into the optical fibre. Because the diameter of the optical fibre is smaller than the diameter of the scintillator, it needs to be focused. The focusing of the light rays can be done by either a mirror or a lens. The light will propagate through transparent parts of the dosimeter during this process. The light loss during transmission must be as low as achievable, preserving the limited scintillation light produced. It is crucial to understand how the light gets lost in both the scintillation crystal and the optical fibre to determine the transmission loss. The optics presented in this chapter will help to understand the light transmission in the OIVD sensor system.

To measure the delivered dose accurately, the optical transmission must be as efficient as possible. To do so, it is relevant to understand the propagation of light described in Section 4.2

### 4.1. Structure of optical fibre

The structure of the optical fibre used for the sensor is shown in figure 4.1. In general, optical fibres consist of three layers that are merged into a cylindrical shape. The three parts of an optical fibre are: The core, the cladding and the jacket. The scintillation light is mainly guided inside the core, the cladding around the core keeps the light in the core due to the relative difference in refractive index, and the jacket is added as a protective layer around the fibre.

The cross-section of the optical fibres is shown in figure 4.2. Here an incident ray enters the core at an angle  $\theta_1$  and is refracted into the core at  $\theta_2$ . When the ray propagates through the core ( $n_1$ ) and hits the cladding ( $n_2$ ) with an incidence angle ( $\theta_3$ ) larger than the critical angle  $\theta_c$ , refraction cannot take place. As a result, the light ray is reflected into the core. This process is called total internal reflection (TIR) and further described in section 4.2.2.

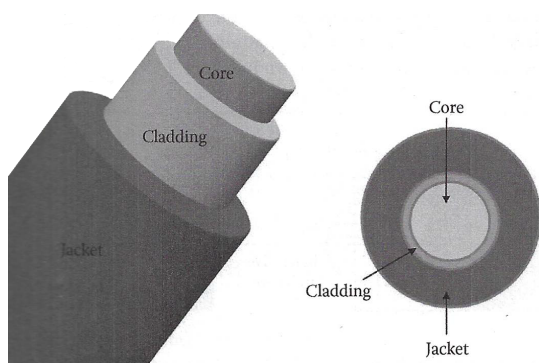


Figure 4.1: Structure of a basic optical fibre

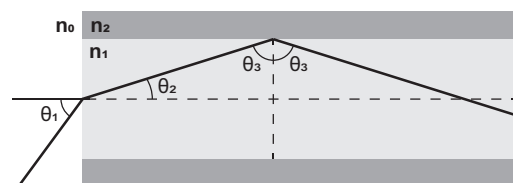


Figure 4.2: An incoming light ray at the maximum acceptance angle enters and propagates through a step index fibre

## 4.2. Propagation of light

Propagation of light is the way an electromagnetic wave transfers through a medium or from one medium to another. Four processes occur when the light propagates are described in this section: Attenuation (4.2.1), reflection (4.2.2), refraction of light (4.2.3), and transmission (4.2.4).

### 4.2.1. Attenuation of light

When light propagates through a transparent medium, it may be absorbed, scattered or both; this is called attenuation (77). The light intensity ( $I_x$ ) must be preserved to transfer as generated scintillation light to the photodetector. The attenuated light can be calculated with the following equation Equation (4.1) (23):

$$I_x = I_0 e^{-\mu x} \quad (4.1)$$

Where  $I_0$  is the incident light intensity,  $\mu$  the attenuation coefficient and  $d$  the thickness of the material, for optical transmission,  $I_x$  should remain high, so the light throughput remains high. More information about scintillators with a low attenuation coefficient can be found in appendix A.

### 4.2.2. Reflection of light

When an incident ray of light hits a reflective surface, it will continue as a reflected ray. There are two laws of reflection: 1. The incident ray, the normal at the point of incidence and the reflected ray lie in the same plane. 2. The angle of incidence is always equal to the angle of reflection. This principle is visualized in figure 4.3a where both the angle of incidence as the angle of reflection is denoted with  $\theta_1$ .

### 4.2.3. Refraction of light

Refraction of light is the bending of a light ray when it goes from one medium to another. This phenomenon does occur because the speed of light in the different mediums are different. The way a light ray bends depends on the index of refraction. The refractive index ( $n$ ) is the ratio of the speed of light in a vacuum ( $c$ ) to the speed of light in a medium ( $v_m$ ) and can be calculated according to equation (4.2).

$$n = \frac{c}{v_m} \quad (4.2)$$

When an incident light ray from the scintillator enters the optical fibre with a different density, the ray will be tilted. The tilted angle depends on the indices of refraction of the two media and is described quantitatively by Snell's Law, see equation (4.3). When the medium  $n_1$  is denser than medium  $n_2$  the light is tilted away from the normal plane, this is visualized in figure 4.3a. Where the angle of the incident light ray is denoted with  $\theta_1$  and the angle of the refracted ray is denoted by  $\theta_2$ .

$$n_1 \sin(\theta_1) = n_2 \sin(\theta_2) \quad (4.3)$$

When the angle of the incident light ray ( $\theta_1$ ) increases to the critical angle ( $\theta_c$ ) the angle of refraction becomes  $90^\circ$ , the reflected light ray will travel in between media and will get lost. This phenomenon is show in figure 4.3b.

When the angle of incoming light ray increases to a value larger than  $\theta_c$ , the ray is totally reflected and stay in the same medium  $n_1$  as shown in figure 4.3c. This phenomenon is called TIR and is one of the principles of light transmission through optical fibres, see figure 4.2 (32).

### 4.2.4. Light transmission

When light hits a transparent or translucent object, a part of the energy is attenuated as described in section 4.2.1. The rest of the light passes through the object and is released on the other side, this is called the transmitted light. The amount of transmitted light can be calculated with the Beer-Lambert equation (4.4). In which the absorbance ( $A$ ) has an inverses exponential relationship to the transmittance ( $T$ ).

$$A = \log \frac{I_0}{I_x} = -\log T \quad (4.4)$$

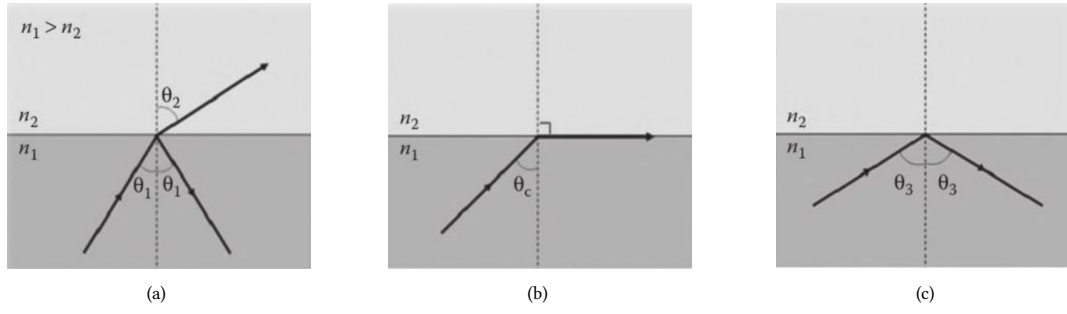


Figure 4.3: (a) Refraction and reflection at the boundary between two media with different refractive indices, (b) critical angle and (c) total internal reflection (10)

### 4.3. Fibre coupling efficiency

Fibre coupling efficiency is the percentage of the generated scintillation light coupled into the fibre. This can be calculated by determining the overlap between the spot focus and fibre core. The fibre core is  $100\mu m$  and is predetermined by Elekta.

The efficiency of Light coupling in a scintillation detector system depends on the shape and quality of its components. The light collection efficiency in the fibre  $\epsilon_{light}$  can be defined as (9):

$$\epsilon_{light} = \epsilon_{\theta_{max}} \epsilon_{couple} \quad (4.5)$$

Where  $\epsilon_{\theta_{max}}$  is the fraction of light photons produced in the scintillator which would enter the fibre within the acceptance cone as described in equation (4.6). The coupling efficiency ( $\epsilon_{couple}$ ) represents the transmitted photons through to coupling between the scintillator and the optical fibre. So the to achieve an efficient coupling focus of the generated light needs to lay in the fibre to increase the  $\epsilon_{in}$ . This can be enhanced by implementing lenses or optical antennas (75, 73). The different materials influence the coupling efficiency between both interfaces, a good optical coupling will transmit roughly 50% of the photons (9).

### 4.4. Acceptance angle of an optical fibre

The acceptance angle is the maximum angle of a ray hitting the fibre axis, allowing the light ray to enter the fibre. This is mainly determined by the numerical apertures (NA), the NA value is used to describe the light ray collection ability of an optical fibre.

Light can only enter the fibre when the incoming angle is within the acceptance cone of the fibre. The acceptance cone is twice the acceptance angle  $\theta_0$  and is related to the NA parameter, shown in figure 4.3c. The acceptance angle is determined by equation (4.6) which is based on the indices of refraction of the core ( $n_1$ ), the cladding ( $n_2$ ), and the medium ( $n_0$ )

$$NA = n_0 \sin(\theta_{max}) = \sqrt{n_1^2 - n_2^2} \quad (4.6)$$

figure 4.4 shows the configuration where an optical fibre with a small diameter is coaxially coupled to the scintillator. Where the scintillator is divided into slices of a thickness ( $dz$ ). The light collected by the optical fibre ( $dP$ ) can be calculated with equation (4.7)(25).

$$dP(r, z) = 2\pi r dr I_0 dz \frac{dA \cos\phi}{4\pi(r^2 + z^2)} \quad (4.7)$$

The total light power collected from the scintillator into the fibre can be found by integrating over  $r$ , and  $z$  (25).

To Mazimize the light coupled into the optical fibre the dosimeter should:

1. Maximise the NA of the fibre.
2. Add a low refractive index cladding to the sides of the scintillators to ensure the TIR or add a reflective coating.
3. Add a reflective coating to both scintillator ends. This will enlarge the effective length of the scintillator.

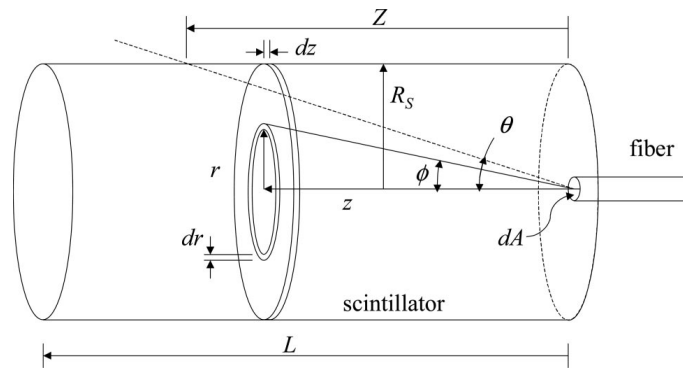


Figure 4.4: An optical fibre coupled to a cylindrical scintillator. An annulus with thickness  $dz$  used in equation (4.7) is shown at the distance  $z$  from the fibre

Another way to improve the light coupling is by the use of optical concentrating elements between the scintillator and the fibre. An added lens magnifies the cross-sectional area of the optical fibre, see figure 4.5 (25).

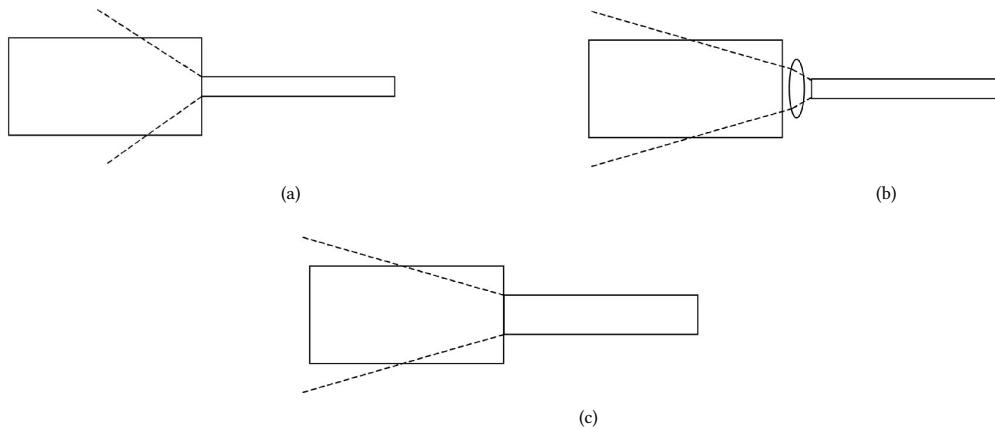


Figure 4.5: a) Acceptance cone of a butt coupled fibre. (b) The lens added results in a change in the NA and magnification of the fibre. (c) The equivalent of the lens added to the system, resulting in a wider optical fibre with a reduced NA(25)

## 4.5. Signal To Noise

To regulate the adequacy and sensitivity of the OIVD sensor, its necessary to determine a definition of the signal to noise (S/N) ratio which is and suitable for applications in *in vivo* dosimetry (IVD) for brachytherapy (BT). All components of the OIVD sensor assembly contributing to the S/N ratio need to be analyzed to determine the adequacy of sensitivity. The photodetector measures the light produced and transmitted. The dominant source of the noise will come from the fibre in the form of Cherenkov radiation. A good subtraction of the noise can be done with a background fibre as described in section 3.6.6. The measurement of the S/N ratio is the most relevant physical characteristic to quantify the efficiency of the optical couplings and measure accurate dose delivery.



# 5

## Method

With the theoretical knowledge in mind, it is possible to select the most suitable scintillator for the optical *in vivo* dosimetry (OIVD) sensor assembly. With this in mind, it is possible to find an answer for the subquestions 3&4 described in section 1.1. Multiple simulations of the head of an OIVD sensor assembly are executed to find the answers. These simulations in COMSOL Multiphysics (CM) help to find the best shape of the scintillator and the minimum thickness of the optical fibre. In section 5.1 an outline is determined for this configuration. section 5.2 describes the physics package needed to make the model function in COMSOL Multiphysics. A parameter set is established in section 5.3 to define the model. This chapter is Finalised by the modelling workflow in CM as described in section 5.4.

### 5.1. Design outline and justifications

In chapter 3 and chapter 4 the theory used for the model was outlined. The chosen configuration is a coated scintillator in a protective capsule coupled into an optical fibre in which the ray's will reach the detector. With this in mind, a 2D outline of the design can be set up, see figure 5.1.

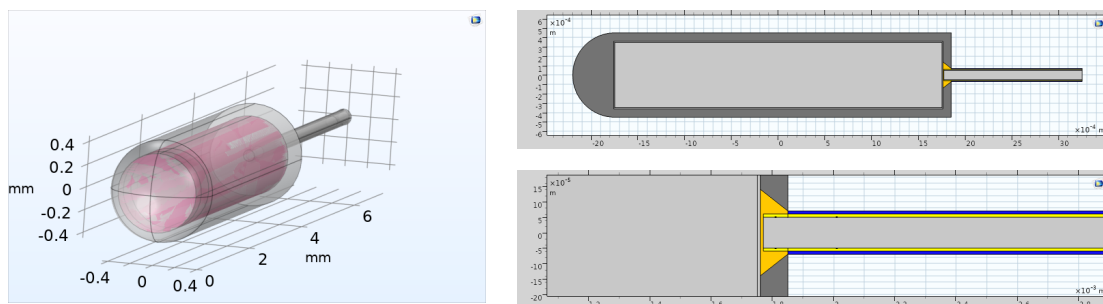


Figure 5.1: The proposed outline in 2D and 3D of the OIVD sensor system design without background fibres

Based on the findings presented in chapter 3 and chapter 4, we can observe a coupled  $ZnSe:O$  scintillator coupled into a relatively small optical fibre. During the design process, the light loss in the cable to the photodetector had no priority, and therefore assume there is no signal loss over the length of the optical fibre. This influenced the efficiency of the total OIVD sensor system, but since the main goal is to get insight into the coupling efficiency between the scintillator and fibre, this model will be sufficient.

### 5.2. Physics of the model

Within the COMSOL multiphysics® software, two packages have been used to model the light transmission in the OIVD sensor system. The ray optics and wave optics package. The software cannot model the scintillation process and the Cherenkov light. However, the program is suited for optimising the light throughput and the coupling efficiency.

### 5.2.1. Ray optics

The geometrical Optics (GOP) interface solves the position and wave vector of individual rays; this allows them to interact with boundaries that intersect their ray paths. The scintillator, capsule and cable are made using multiple build-in geometries from COMSOL. This is both done in 2 and 3-dimensional geometry. The ray optics module is a computational tool that simulates the propagation, reflections, refractions and absorption of light with a ray-tracing approach. All of these features are available in the GOP interface, so the light intensity and power can be in the OIVD sensor assembly can be calculated and compared.

Next to this, it is possible to adjust the wavelength parameter of the exited rays and where and in which direction these are released. With the Fresnel equation, it is possible to assign multiple boundary conditions to all surfaces in the geometry to solve the ray paths for rays as they cross a boundary between two media with different refractive indices.

With the COMSOL multiphysics, it is possible to combine the ray heating (RH) with the GOP interface. This RH interface could solve the heat transfer in a domain caused by radiation absorption. Note that x-ray and  $\gamma$ -ray modelling may require the consideration of diffraction effects because they interact with matter on an atomic level.

### 5.2.2. Wave optics

To reduce computational effort, the computational time of the ray-tracing model is compared to the wave optics model. This model requires a numerical method that can solve problems in the field of electromagnetic waves at optical frequencies. This is done with a full-wave propagation method that is based on Maxwell's equations. Both the section 5.2.1 and section 5.2.2 methods are based on the finite element method (FEM).

## 5.3. Parameter identifications

To come to a design with a maximum light coupling efficiency, multiple parameters were defined to come to a full OIVD sensor assembly. The parameters are divided into three categories. First, the parameters of the scintillation crystal; some of these operational parameters can be changed to some extent. Others are predetermined during the fabrication process. Next, the connection properties are studied. These are the size of the protective capsule, the thickness of the optical fibre, and the optical glue's viscosity. Finally, the shape of the optical fibre is studied, which contains the fibre ends, diameter, cladding thickness, and material.

### 5.3.1. Operational parameters

The operational parameters are the source power ( $P_{src}$ ), cable diameter ( $d_{cab}$ ) and coupling shape. These are all flexible during the simulations. The light power of the scintillator depends on the selected scintillator, the distance to the radioactive source and the type and age of the source. However, only limited data is available in the literature. Therefore, the ratio between the different assemblies is more important than the actual source power. There are multiple commercially available optical fibres with a sub-millimetre cross-section. However, not all optical fibres can withstand radiation. Therefore the PMMA fibre used for the experiments by E.Andersen is unsuitable. The Ge-doped fused Silica-doped fibre by CeramOptec is used for the final model.

To my knowledge, it is not clear what the minimum diameter is to have sufficient light throughput, and therefore the ( $d_{cab}$ ) parameter is one of the most important ones in the presented simulations. As stated in chapter 4 there is only little data available for optimizing shapes for OIVD, so this desires simulations of the coupling efficiency for different scintillator shapes.

### 5.3.2. Scintillator parameters

The scintillator dimension parameters are the width ( $w_{sci}$ ) and height ( $h_{sci}$ ) of the scintillator, the refractive index ( $n$ ), the imaginary part of the refractive index, which handles the attenuation ( $\kappa$ ) and the exited wavelength ( $\lambda$ ). Together they account for the total amount of light photons reaching the photodetector. And therefore have great influence on the feasibility of the OIVD sensor assembly. As mentioned in chapter 3, the volume of the scintillator relate to the total amount of light excited due to scintillation. Despite this, it is not possible to exceed the dimension as mentioned in the sketch shown in figure 2.1b. The best-suited scintillation materials for OIVD are available in the COMSOL material libraries as host materials. However, these materials are undoped and vary from the tested properties in the literature. That is a common problem for simulations because material properties differ depending on grades, heat treatment and composition. Therefore some materials need to be adjusted to match the literature.

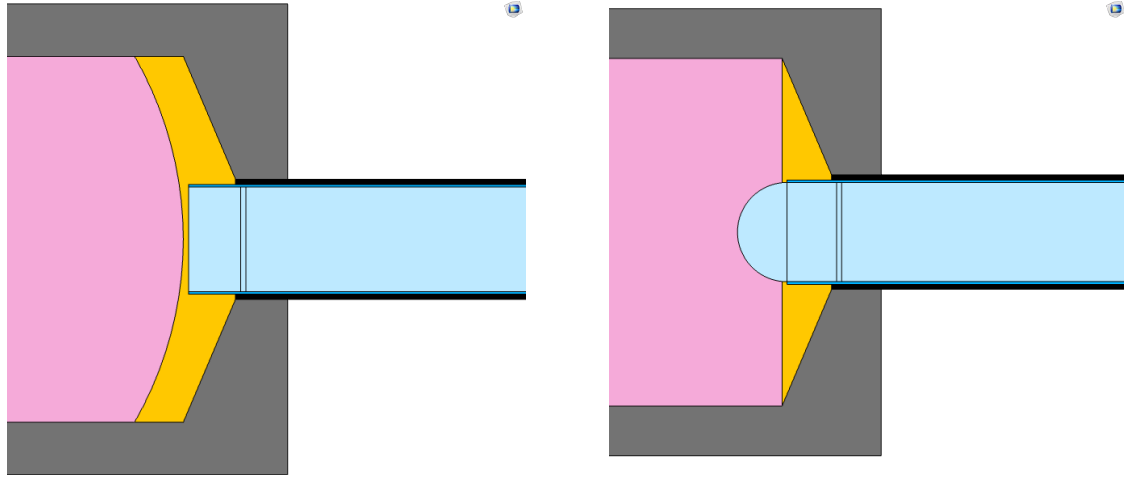
---

The exited wavelength depends on the energy of the exited  $\gamma$ -ray of the  $^{192}\text{Ir}$  source and the type of scintillator. According to the publications presented in chapter 3 the exited wavelength varies from 400-700 nm.

### 5.3.3. Coupling parameters

Finally, all geometries have multiple parameters to determine how the scintillator is coupled. Two examples are given in figure 5.2. The coupling parameters and their dimensions are key factors for the light throughput to the detector outside the patient. The way the cable has recessed, the diameter and the type of optical glue play a key role in the light coupling efficiency. Since they need to have a wide numerical apertures (NA) and low attenuation ( $\kappa$ ).

The cable diameter ( $d_{cab}$ ) is likely to remain  $<200\mu\text{m}$  because of the need for a background fibre. However, there are other filter methods to remove the stem effect in the fibre. In addition, an optical adhesive with a low viscosity is needed to attach the scintillator to the optical fibre. The Preloaded Nordland from Edmund optics suits best for this task and is applied in all models due to their high refractive index and low attenuation (61).



(a) The scintillator head is shaped like a ball lens to focus the exited light in the optical fibre

(b) The optical fibre is partly recessed in the scintillator, which increases the NA of the optical fibre

Figure 5.2: Coupling geometries of two selected simulations, the pink colour represents the scintillator, the orange the optical adhesive and the cyan the fibre core

## 5.4. Modelling work flow

With presented physics and parameters the model can be defined in the COMSOL 2D model builder. During this research, both 2D and 3D models were designed to verify the mechanism and coupling efficiency of the OIVD sensor assembly. Because of the computational burden and the axisymmetrical geometry, only the 2D model is been included in this thesis. The modelling workflow of the OIVD sensor assembly is as follows:

1. In the global definitions node, all geometrical dimensions are defined, including some dependent variables such as the wavelength and light intensity exited from the scintillator.
2. The geometry is based on literature findings as described in chapter 4 and section 5.1 It can be divided into four domains: The scintillator, the protective capsule, the coupling and the optical fibre to bring the signal to the photodiode.
3. The parts of the four domains contain six materials: the AISI 316L Stainless steel capsule, the aluminium oxide ( $Al_2 : O_3 : Cr$  inorganic scintillator, the preloaded Nordland optical adhesive, the PMMA fibre with silicon cladding and a polymer jacket. The optical coatings in the model are replaced with material discontinuities because the results are similar and they reduce the computational time.
4. This is followed by the geometric optics where the optical rays are released in a grid, the medium and ray properties are assigned, the material discontinuity is adjusted and multiple image planes are assigned to read out the data.
5. The physics used in the model and the type of study are assigned next. This is done with a parametric sweep and ray tracing.

6. Finally an extremely fine physics controlled mesh is applied to the model. Since it is of the greatest importance to trace the rays precisely over the material edges.

## 5.5. literature background for the design

The OIVD sensor assembly is defined by looking more closely at examples from experimental setups described in the literature. In section 5.5 the technical details are summarised.

| Scintillation material | Scintillator volume (mm <sup>3</sup> ) | Cable core diameter (mm) | Exited wave-length peak ( $\lambda$ ) | Other remarks  | Ref. |
|------------------------|--|--------------------------|---------------------------------------|--|------|
| BCF-12                 | 0.8                                    | 1                        | 435                                   | Organic scintillator by Saint Gobain<br>(~ 8000 Photons per MeV) | (47) |
| BCF-60                 | 0.8                                    | 1                        | 530                                   | Organic scintillator by Saint Gobain<br>(~ 7100 Photons per MeV) | (81) |
| $Al_2O_3 : C$          | 0.5                                    | <1                       | 511 & 694                             | Grown by Landauer Inc. (USA)<br>using the Czochralski technique  | (6)  |
| $Al_2O_3 : Cr$         | 0.26                                   | 1                        | 694                                   | Produced by Edmund Optics  | (47) |
| $CsI : Tl$             | 1.00                                   | 1                        | 550                                   | Grown by SICCAS<br>Refractive index n=1.78                       | (47) |
| $SiO_2 : Ce^{3+}$      | 0.38                                   | 0.22                     | 611 & 694                             | Produced by Starlite Srl   | (16) |
| $YVO_4 : Eu^{3+}$      | 0.5                                    | <1                       | 611 & 694                             | Compound in powder form<br>produced by Phosphor Technology       | (55) |
| $ZnSe : 0$             | 1.00                                   | 1                        | 590                                   | Grown by ZnSe:O ISMA<br>Refractive index n=2.66                  | (47) |

Table 5.1: Design specification of eight OIVD sensor assemblies

The design for the COMSOL simulation in this thesis will be using a mixture of techniques shown in the articles presented in section 5.5. The table shows examples of OIVD sensor assemblies with scintillation crystals or scintillating fibres. These articles teach us the following things:

1. Most of the current experimental setup for OIVD sensors uses inorganic scintillators.
2. The exited photon wavelengths from the scintillation materials are distinguishable from Cerenkov radiation.
3. The scintillation volume that fits in the head of the  $^{192}Ir$  capsule is larger than the scintillation volume used in literature.
4. The optical cables used in the literature is larger than the desired 300  $\mu m$ , so an additional fibre for the reflection measurements and a background fibre won't fit in the transfer tubes.
5. Non of the articles presents an exact number of photons for accurate dose measurement.
6. Non of the articles uses an optimised shape to have a high photon transmission in the coupling, desired for accurate dosimetry.



# 6

## Simulations

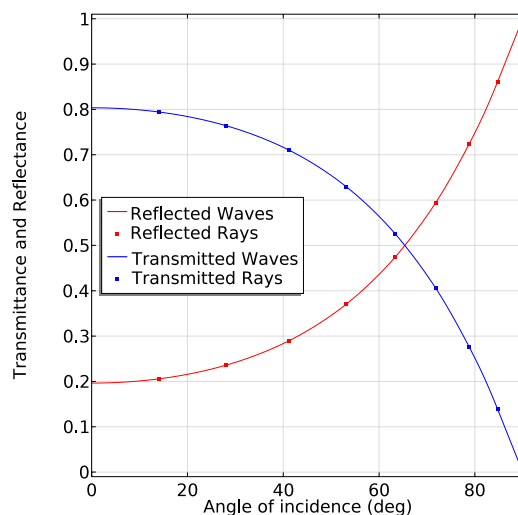
In this chapter, multiple simulations of the coupling mechanism are executed in COMSOL Multiphysics (CM)®. To validate the ray-tracing package, a comparison with the wave- and ray-optics are performed so the behaviour of light at the transition between materials can be checked; this is described in section 6.1. After that, the results need to be extracted, so the model needs to be evaluated in section 6.1.1. This is followed by a parameter study which set the expectation for the creation of the final optical *in vivo* dosimetry (OIVD) sensor system presented in section 6.2.

### 6.1. Model verification

The boundary condition of the OIVD model are defined in chapter 5. The cable thickness and shape parameters need to be validated to finalise the model. The CM can determine the light transmission with the Maxwell equation in the wave-optics module or snells laws with the ray-optics module to determine which model works best; both models are compared, and the results are shown in figure 6.1. The results are similar when observed in a model according to figure 6.1a, where a parameter sweep over the incoming angle (0-90°) are evaluated without attenuation.



(a) The 2D model to find the reflectance and transmittance of the angle of incidence, by releasing rays in 360° at the boundaries between the scintillator and fibre. The blue halves represent the  $Al_2O_3$  scintillator, and the grey halves the PMMA fibre



(b) Reflectance and transmittance as functions of the angle of incidence

Figure 6.1: The behaviour of an incoming light ray at the material transition from scintillator to fibre without attenuation, both executed in the ray- and wave-optics module in COMSOL Multiphysics

In order to verify the behaviour of the rays over the whole OIVD sensor, the refractive index is evaluated. After that the behaviour of the rays is studied in section 6.1.1 and section 6.1.2. This is followed by the intensity

calculations, which are based on the formulas described in chapter 4 and the Finite Element Method (FEM) described in section 6.1.3.

### 6.1.1. Refractive index and attenuation coefficient of the suitable scintillators

As described in chapter 3 there are multiple scintillators suitable as a light-generating device for an  $^{192}\text{Ir}$  source. Nonetheless, most literature do not go into the behaviour of light in the crystal and at the boundaries. This is evaluated in a CM model where both wave- and ray optics are compared with the available literature. This is required because the crystals used in the CM model are undoped materials. The optical properties of materials will change under the influence of dopants as described in section 3.6.5, so some material parameters need to be adjusted before they can be implemented. A summary of the literature and an overview from the CM data are shown in table 6.1. In figure B.3 and figure B.4 the results are obtained for the reflection, transmission and absorption of the CM models as described in section 6.1.

| Material                           | Refractive index at peak wavelength (n) | absorption coefficient (k) | Ref.      |
|------------------------------------|---|----------------------------|-----------|
| $\text{Al}_2\text{O}_3 : \text{C}$ | 1.77                                    | 0.1-0.3                    | (46) (34) |
| $\text{Al}_2\text{O}_3$ - (CM)     | 1.75                                    | 0.02                       | (53)      |
| $\text{CsI} : \text{Tl}$           | 1.79                                    | 0-0.1                      | (65)      |
| $\text{CsI}$ - (CM)                | 1.71                                    | N/A (0)                    | (83)      |
| $\text{NaI} : \text{Tl}$           | 1.85                                    | N/A (0)                    | (64)      |
| $\text{NaI}$ - (CM)                | 1.94                                    | N/A (0)                    | (40)      |
| $\text{Y}_2\text{O}_3 : \text{Eu}$ | 1.7                                     | N/A (0)                    | (57)      |
| $\text{Y}_2\text{O}_3$ - (CM)      | 1.93                                    | N/A (0)                    | (60)      |
| $\text{ZnSe} : \text{O}$           | 2.66                                    | N/A (0)                    | (39)      |
| $\text{ZnSe}$ - (CM)               | 2.58                                    | 0.06                       | (2)       |

Table 6.1: Refractive indices and absorption coefficients of multiple materials, CM stands for the build-in material in COMSOL Multiphysics

### 6.1.2. Reflective coating

A reflective coating is a thin layer applied to the surface of an optical device such as a scintillator to increase reflection. The increase of reflected light leads to a higher light throughput in the optical fibre and increases the efficiency of the optical system. The reflectance of the think layer depends heavily on the angle of incidence of the light, because total internal reflection (TIR) is desired.

When the light with a wavelength ( $\lambda=620\text{nm}$ ) goes from the ruby ( $n_1=1.75$ ) to the Stainless steel capsule ( $n_2=2.76$ ) a thin layer ( $n_f$ ) made with a high refractive index should be used to get a high reflective coating ( $n_c$ ), see section 6.1.2.

$$n_c = \sqrt{\frac{n_1 \cdot n_f^2}{n_2}} \quad (6.1)$$

The reflective coatings showed in section 6.1.2 are tested in CM, and the reflectance of the zirconium Oxide ( $\text{ZrO}_2$ ) film on a ruby is shown in figure 6.2.

| Material       | Refractive index (n) |
|----------------|----------------------|
| $\text{MgF}_2$ | 1.38                 |
| $\text{SiO}_2$ | 1.46                 |
| $\text{CeF}_3$ | 1.63                 |
| $\text{ZrO}_2$ | 2.2                  |

Table 6.2: Refractive indices of coating materials



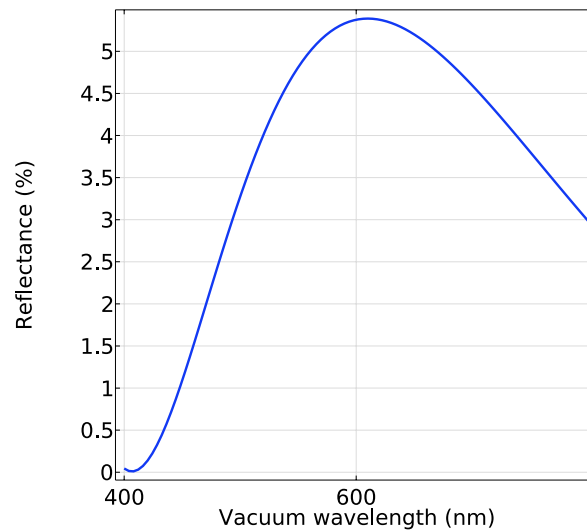


Figure 6.2: Reflectance of zirconium oxide layer between a ruby and the stainless steel capsule when a light ray hits the stainless steel capsule perpendicular

### 6.1.3. Finite Element method

The FEM modifies the solver and the computational burden. First, the domain of interest is divided in a finite element mesh with geometrically simple finite shaped element, see figure 6.3a. The size of the triangle in the mesh is calculated by the use of lagrangian interpolations (18). One of the major advantages of FEM is that multiple sized meshes will help to reduce the computation time while preserving accurate results, e.g. a more refined mesh at specific parts of the CM model, such as the transition between material. Increasing the number of elements by refining the mesh improves the solution accuracy but increases the computational burden. For the models presented in chapter 7 an extremely fine is used because the CM model is evaluated in 2D, and the transmission efficiency is below the 5%.

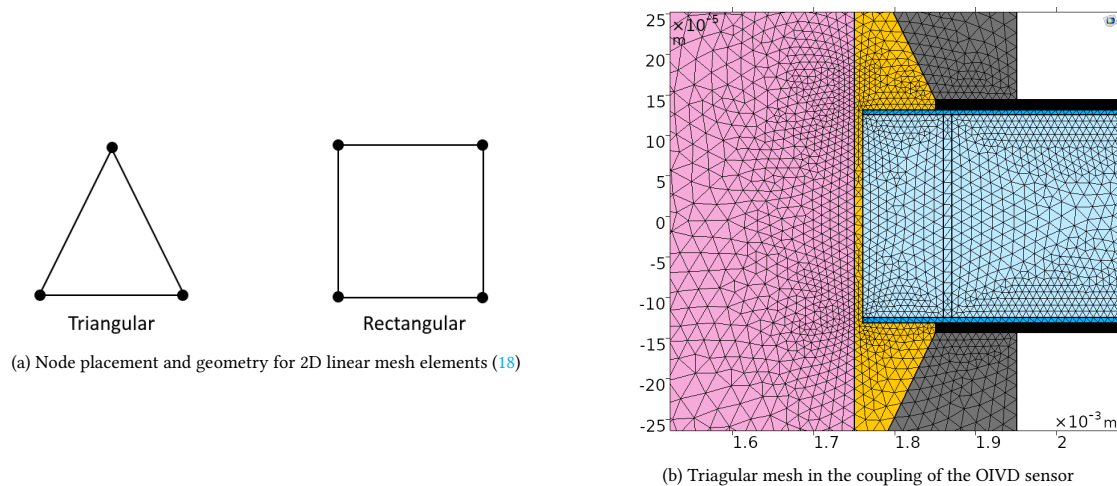


Figure 6.3: A dedicated mesh size for the individual domains

### 6.1.4. Coupling efficiency of the fibre

An essential part of this study is the coupling efficiency. This is a parameter that is essential for the fabrication of the OIVD sensor system. In section 6.2 the coupling efficiency is shown as a function of the diameter. 17640 rays are released from a 7x35 grid to determine the coupling efficiency, and a part of them will reach the detector. However, most rays will be partly reflected and transmitted and lose energy with their interactions, but the number of rays increases. Only the rays with more than 10% of the initial power (W) will be processed to limit the computation time. This means that more than 100% of the rays can reach the detector in theory. To

get insight in the coupling efficiency of the CM model a section 6.1.4 with the coupling efficiency is presented with the coupling efficiency of the CM model with a capsuled  $Al_2O_3$  is shown. This helps to get insight in finding the geometry of the OIVD model.

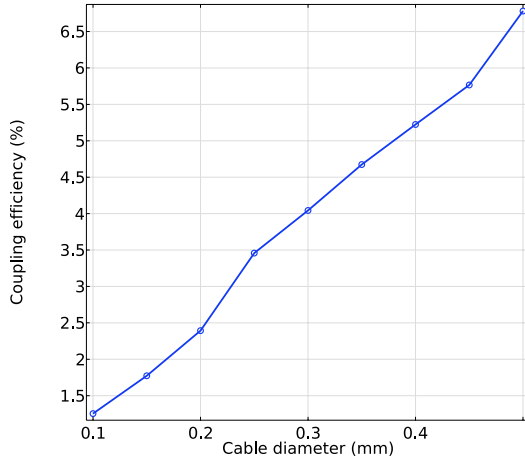


Figure 6.4: The coupling efficiency of the model presented by E. Andersen (5) as a function of the diameter of the optical fibre

| Diameter fibre (mm) | Rays reaching detector | Light intensity at detector (%) |
|---------------------|------------------------|---------------------------------|
| 0.10                | 1073                   | 6.08                            |
| 0.15                | 1565                   | 8.87                            |
| 0.20                | 2105                   | 11.93                           |
| 0.25                | 2681                   | 15.20                           |
| 0.30                | 3179                   | 18.02                           |
| 0.35                | 3643                   | 20.65                           |
| 0.40                | 4068                   | 23.06                           |
| 0.45                | 4500                   | 25.51                           |
| 0.50                | 4958                   | 28.10                           |

Table 6.3: The number of rays and the light intensity entering the optical fibre compared with the cable diameter. The initial number of rays released in the scintillator is 17640.

## 6.2. Configuration of the OIVD sensor assembly

The literature shows that there are multiple ways to design an OIVD sensor system; the most basic model is inspired by the model by E. Andersen (5). The same stainless steel capsule encapsulates this model as the  $^{192}Ir$  source presented in chapter 2. To connect the inorganic scintillator with the PMMA fibre, the adhesive Norland Optical Adhesive (NOA61) is used with a viscosity of 300 cps. The PMMA fibre modelled in CM is the commercially available (ESKA GH2001-P) produced by Mitsubishi Rayon Co. Modelled with a variable core diameter (0.1-0.5 mm).

Literature shows that the commercially available Ge-Doped fused Silica-doped fibre by CeramOptec has better performance, and therefore a better choice for the OIVD sensor system. However, comparing the system with the model presented by E. Andersen, the same PMMA fibre is used.

The model was consistent with the refractive index and absorption findings in simulations presented in the literature. However, there is a parameter unclear from all literature. Which is the minimum required light yield throughput to OIVD sensor system to make it suitable for clinical use. Multiple papers conclude with: " This phantom-based study showed that the tested  $Al_2O_3$  : C OIVD system performed well in a brachytherapy environment with  $^{192}Ir$  as the radiation source." (5). Which makes it hard to validate the CM models. All data is given in % of the initial light intensity to compare in the same way, without knowing the minimum required light yield. The in model presented in figure 6.5 is used for the graph in figure 6.6 which show the first result of the CM model.

The fabrication and actual testing of these models is beyond the scope of this project, but recommendations for future research are presented in chapter 10.

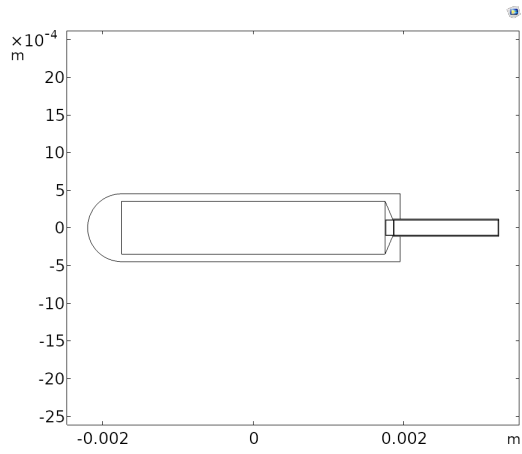


Figure 6.5: The COMSOL model with capsule and  $Al_2O_3$  scintillator

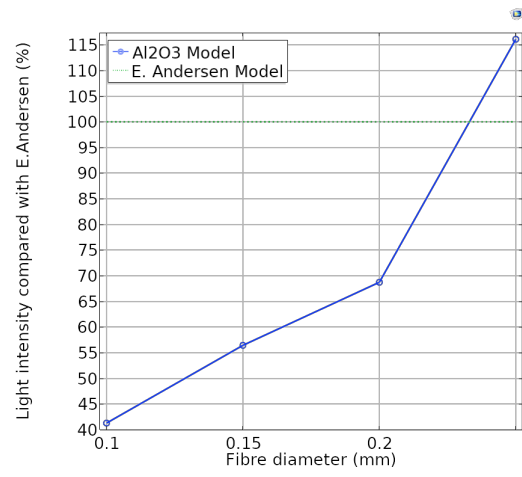


Figure 6.6: The model with capsule compared with the model described by E.Andersen



# 7

## Results

The final design option is presented and justified in this chapter. All designs are shown, and multiple simulations confirm the model properties. First, the designs are compared in section 7.1. This is followed by the light transmission in COMSOL Multiphysics (CM) and Concluded with a comparison of the CM models.

### 7.1. Design overview

The designs presented in section 7.1 are based on literature presented in chapter 4. The optical fibre in all models are connected with the adhesive Norland Optical Adhesive (NOA61).

| optical <i>in vivo</i> dosimetry (OIVD) model    | Scintillator width (mm) | Scintillator volume( $mm^3$ ) | Coupling                          | Cable cross section ( $mm^2$ ) | <i>in vitro</i> tested |
|--|-------------------------|-------------------------------|-----------------------------------|--------------------------------|------------------------|
| <i>Al2O3</i> : C by E. Andersen (5)              | 2                       | 1.56                          | flat: with optical adhesive NOA61 | 0.78                           | yes                    |
| COMSOL model inspired by E. Andersen 7.1a        | 3.5                     | 1.3475                        | flat: With NOA61                  | 0.07-0.28                      | no                     |
| COMSOL model with capsule 7.1b                   | 3.5                     | 1.3475                        | flat: With NOA61                  | 0.07-0.28                      | no                     |
| COMSOL model with cone coupling 7.1c             | 3.5                     | 1.312-1.330                   | cone: With NOA61                  | 0.07-0.28                      | no                     |
| COMSOL model with a halve ball coupling 7.1d     | 3.5                     | 1.234-1.343                   | ball lens: With NOA61             | 0.07-0.28                      | no                     |
| COMSOL model with a recessed cable coupling 7.1e | 3.5                     | 0.802-1.287                   | recessed: With NOA61              | 0.07-0.28                      | no                     |
| COMSOL cable positioning model 7.1f              | 3.5                     | 1.3475                        | flat: With NOA61                  | 0.126                          | no                     |

Table 7.1: Design overview of the COMSOL models

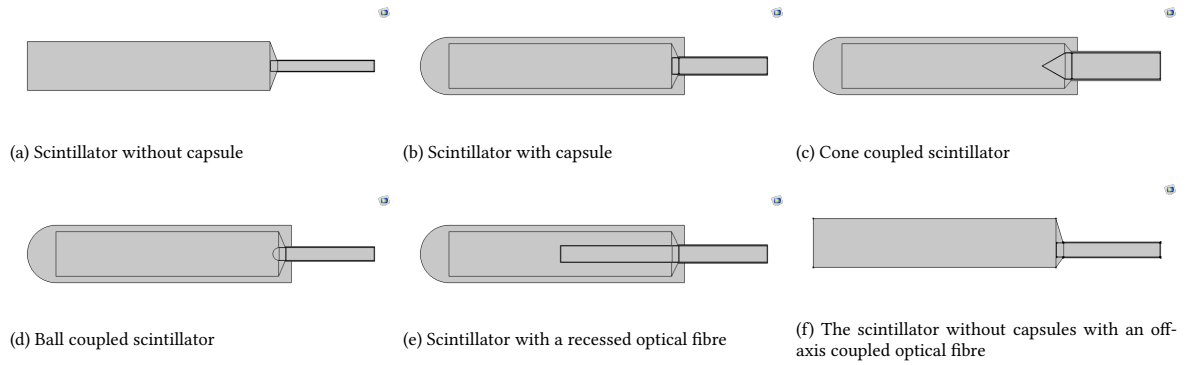


Figure 7.1: Design overview of the COMSOL models to investigate the coupling efficiency

## 7.2. Light transmission in the COMSOL Multiphysics models

In the COMSOL ray optics module, it is possible to solve the position of the wave vector for all the individual rays released from the initial position. From that moment on, the rays move through the mesh element and interact with all boundaries that intersect their path until the rays have  $>10\%$  of their initial value.

While propagating through a homogeneous scintillator, the rays go straight with a speed of  $(c/n)$ . The time-dependent study steps determine where the ray is in the volume. For this research, only the last time step is used. At this moment, the solver accurately interpolates the rays' intermediate time steps. When the rays go through a ray-boundary interaction (e.g. when the ray leaves the scintillator and enters the glue), the ray is stored and available for post-processing. In the simulation, reflection, refraction, and absorption occur. Figure 7.2 show these effects on two modelled scintillators in CM. The absorbance of the  $Al_2O_3$  matches the literature (71).

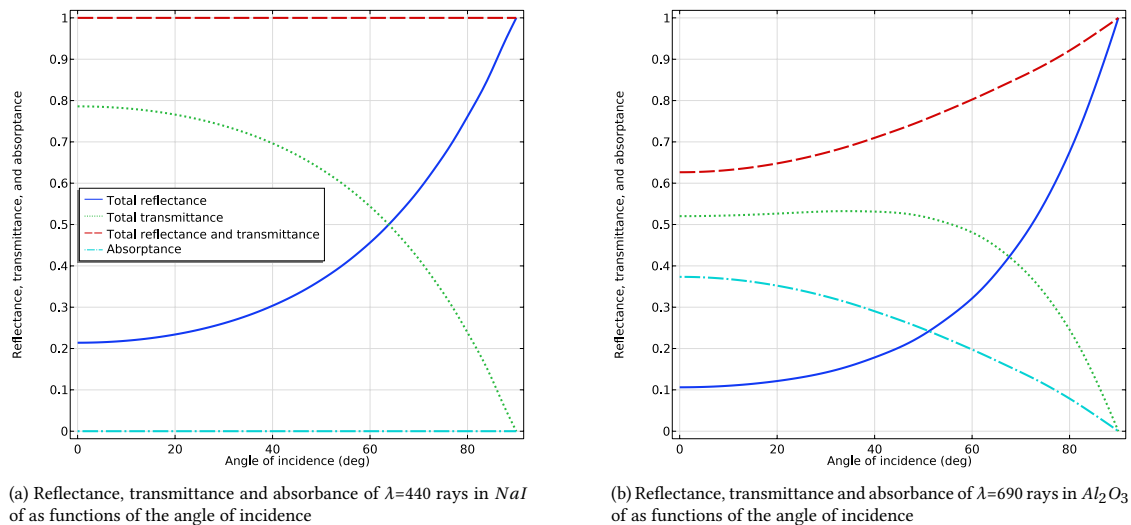


Figure 7.2: The behaviour of an incoming light ray at the material transition from scintillator to fibre without attenuation, executed in the ray-optics module in COMSOL Multiphysics

### 7.2.1. Luminescence in COMSOL Multiphysics

As described in chapter 3 the amount of light generated in the scintillator is depended on the type of scintillator, source type and age, and distance to the scintillator. COMSOL multiphysics cannot simulate this effect. Therefore another method is chosen.

The luminescence centres in the scintillators earlier described as dots are the places in the crystal where most of the light is emitted. A grid is made from where the light rays emitted in the COMSOL model, see figure 7.3a. However, due to the limited computational time, the grid is simplified and turned into a  $7 \times 35$  grid that emits 72 rays per grid point. Along each ray emitting from the grid, it is possible to evaluate expressions, such as

intensity, the wavelength of the ray and optical path length.

### 7.2.2. Positioning of the optical fibre

The optical fibre is used as light-conducting components in the OIVD sensor assembly to bring the scintillation light to the measuring device outside the patient. When the scintillating light enters the optical fibre at a different angle, the coupling efficiency changes, and therefore the fibre must be precisely positioned so the coupling efficiency can be maximised.

Next to this, it is desired to have three fibres connected to the OIVD sensor system. One for the collection of the scintillation light, one for the reflection measurement and the last one as background fibre for the Cherenkov radiation. Due to the limited space available, it is impossible to couple them all in at the centre of the scintillator, so they have to be coupled off-centre. In figure 7.3 we see the scintillation light arising in the form of 72 rays per grid point. The rays are released in an evenly distributed 7x35 grid to limit the computational burden and coupled into a PMMA fibre. In figure 7.3a the fibre is coupled at the centre of the fibre and in figure 7.3a at the sides. The light coupling efficiency (%) can be observed in figure 7.4. This shows that the coupling efficiency is lowest when coupled in the centre of the cylindrical scintillator. However, due to the limited amount of grid points, it can be observed that only 1 row of points lies in line with the coupled fibre when the fibre is shifted downwards, the light reaching the scintillator first increases and later decreases as expected from the knowledge from chapter 4.

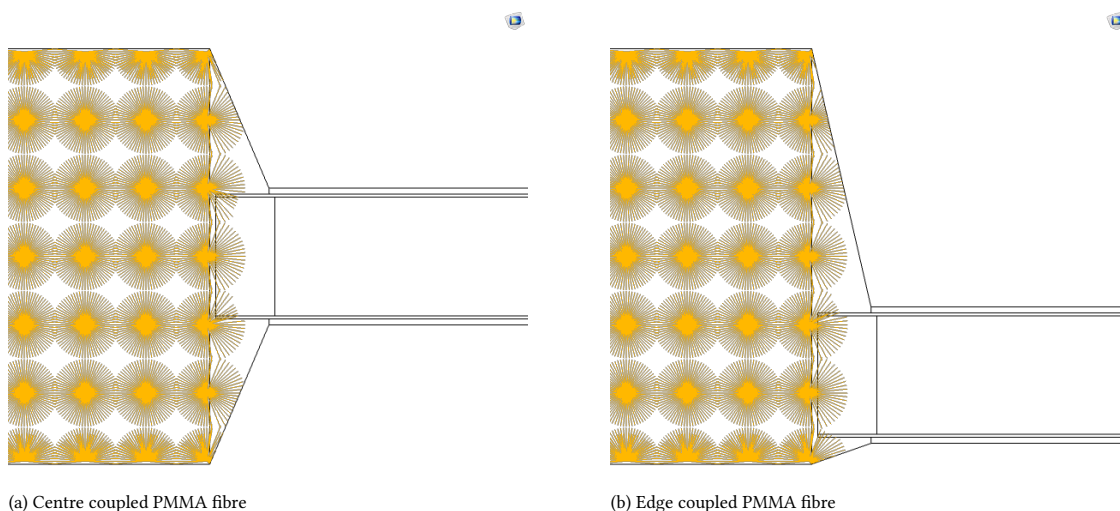
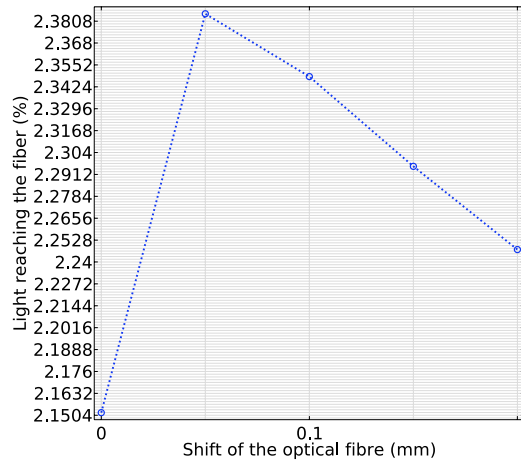
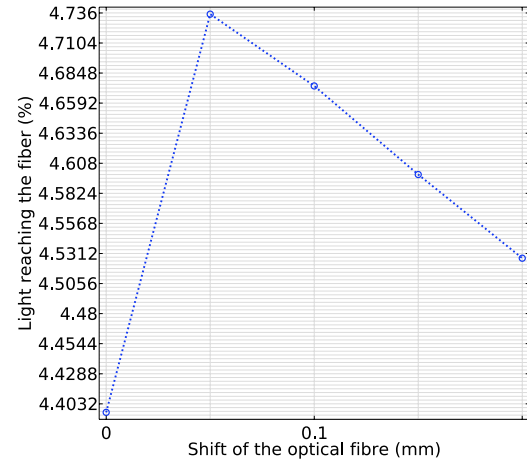


Figure 7.3: OIVD model inspired by E. Andersen

### 7.2.3. Coupling between the scintillator and the optical fibre

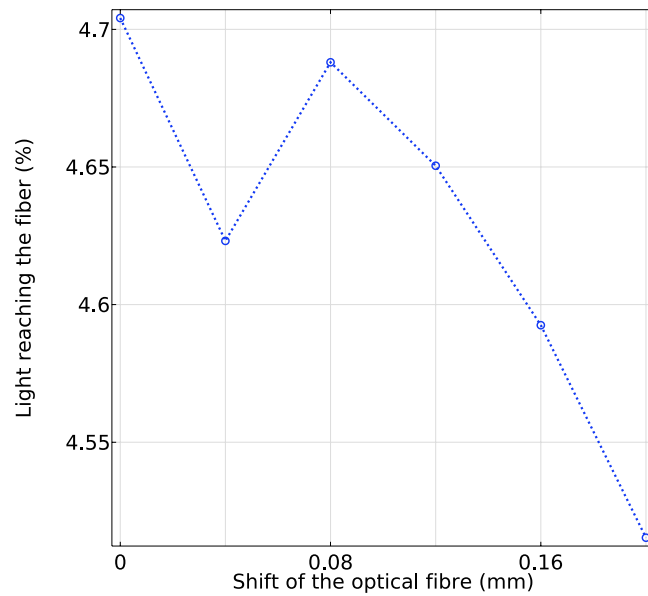
The optimal coupling parameters ensure that the required light yield will reach the detector. figure 7.4b show the coupling efficiency where the attenuation of all parts of the OIVD sensor assembly are manual set to 0. This increases the coupling efficiency and shows that increasing the scintillation volume with a scintillation crystal with a low attenuation coefficient will increase the light throughput in the sensor.

The centre coupled optical fibre has the worst coupling efficiency, which is not obvious. This phenomenon is caused by the odd distributed grid points that negatively influence the coupling efficiency of the centre coupled fibre. Therefore an adjusted grid is used for the fibre position simulation only to see if this result is an outlier. figure 7.5 show the results for the the same model as figure 7.4, but with 28 instead of 7 vertical grid positions.

(a) The attenuation of  $\lambda = 610nm$  light in a  $Al_2O_3:C$  scintillator

(b) without attenuation

Figure 7.4: Light coupling efficiency at the entrance of the PMMA fibre

Figure 7.5: The attenuation of  $\lambda = 610nm$  light in a  $Al_2O_3:C$  scintillator. With an adjusted 28 vertical grid points in the y-direction instead of 7.



### 7.3. Comparison of the COMSOL OIVD models

The CM models give insight into the possible improvements for the OIVD sensor assembly, such as which coating should be used with which geometry does the  $Al_2O_3 : Cr$  scintillator has a maximum light throughput. As observed in table 7.2 the light yield of the  $ZnSe : O$  scintillator is 12x higher than the  $Al_2O_3 : Cr$  scintillator where all CM models are based on. With this in mind, the ball coupled geometry is tested with new materials, the scintillator is material is replaced with  $Al_2O_3 : Cr \rightarrow ZnSe : O$  and the optical fibre is replaced with  $PMMA \rightarrow$  Optran®Ultra WFGE. The results look promising. According to table 7.2 model of the presented ball coupled  $ZnSe : O$  scintillator has a 165.5% better performance than the  $Al_2O_3 : Cr$  model based on the results from E.Andersen (5).

|  | $Al_2O_3 : Cr$ model | $ZnSe : O$ model |
|--|----------------------|------------------|
| Light power released in the scintillator (W)               | 4.94                 | 59.88            |
| Light power reaching the detector (mW)                     | 21.02                | 628.07           |
| Percentage of the released power reaching the detector (%) | 0.40                 | 1.05             |

Table 7.2: Light coupling efficiency

When observing section 7.3, its clear that the use of a fibre with a diameter  $250\mu m$  will give better results than the model presented by E. Andersen 7.1a. Next to that the COMSOL model with the have ball coupling has the best coupling efficiency and is recommended to use for further research.

| OIVD model   | Scintillator volume (mm <sup>2</sup> ) | Cable diameter (mm) | Rays reaching the detector with $\geq 10\%$ of their initial power | Light intensity at detectorm (mW) | Light intensity relative to E. Andersen (%) |
|--|--|---------------------|--|-----------------------------------|---|
| COMSOL model inspired by E. Andersen 7.1a            | 1                                      | 0.5                 | 3983   | 2.782                             | 100   |
| COMSOL model with capsule 7.1b                       | 2.45                                   | 0.2<br>0.25         | 5844<br>7584   | 1.909<br>3.225                    | 68.6<br>115.9                               |
| COMSOL model with cone coupling 7.1c                 | 2.43<br>2.42                           | 0.2<br>0.25         | 6166<br>7774   | 0.872<br>17.88                    | 31.3<br>642.7                               |
| COMSOL model with a halve ball coupling 7.1d         | 2.43<br>2.43                           | 0.2<br>0.25         | 6044<br>7660   | 0.962<br>21.02                    | 34.6<br>755.6                               |
| COMSOL model with a recessed cable coupling 7.1e     | 2.24<br>2.32                           | 0.2<br>0.25         | 7560<br>7560   | 1.561<br>2.704                    | 56.11<br>97.20                              |
| COMSOL model with ZnSe:O and Optran®Ultra WFGE fibre | 0.2                                    | 2.45                | 9600   | 628.1 <sup>a</sup>                | 22577.3                                     |

Table 7.3: light coupling in the COMSOL models

<sup>a</sup>The energy of the released rays in this model is 12 times higher than the rays emitted from the  $Al_2O_3 : Cr$  scintillator, see section 3.7.1



# 8

## Discussion

This chapter will examine the proposed design in terms of the requirements mentioned in chapter 1. As explained, the design met scintillation properties and light coupling efficiency requirements. A summary of the main requirements is presented in table 8.1, onto which a discussion will follow.

### 8.0.1. Optical validation of the COMSOL model

The optical validation is based on the requirements presented in chapter 1 and budget. All values of the COMSOL Multiphysics (CM) are compared with the literature. What can be noticed in table 8.1 is that not all data parameters presented in the literature can be tested in the models. However, some differences need to be explained. The optical transparency of the COMSOL models is different from the literature due to the missing *Cr* dopant in the ruby.

Three conclusions can be drawn from observing the results. First of all, the coupling efficiency of the optical *in vivo* dosimetry (OIVD) is sufficient compared to the model from E. Andersen. However, the way grid points are set to influence the results may cause significant errors in the model.

Secondly, the fibre diameter needs to be reduced. The simulations show similar results can be obtained by increasing the scintillation volume and using an optical fibre between 0.2-0.25 mm. This is mainly influenced by the amount of light generated at the coupled half of the scintillator. Most of the rays have multiple boundary interactions before they reach the optical fibre, and because all rays with <10% of the initial energy are discarded, the experimental results can differ from the simulations.

Thirdly, the current implementation of the OIVD sensor assembly in CM is not suited because the excitations and the amount of light produced in the scintillator can not be implemented. This causes significant differences from experiments because the amount of generated light depends on the activity of the source, source type and distance to the source.

Overall the table 8.1 shows that the use of ZnSe:O gives the best results within the given requirements.

|                                 | Requirement          | Experimental results by E.Andersen (5) | Final COMSOL Model | Proposed   |
|---------------------------------|----------------------|--|--------------------|--|
| Excited wavelength              | 550-1000(nm)         | 610                                    | 663                | $\pm 600$ ,<br>The excited wavelength must be distinguishable from Cherenkov radiation. The maximum wavelength is not fixed but is limited by the detector outside the patient. (11) |
| Decay Time                      | $\leq 1000\text{ns}$ | 33                                     | N/A                | $\pm 100\text{ns}$ ,<br>The dose needs to be measured multiple times to have an accurate dose measurement.(10)   |
| Position accuracy               | $\leq 2\text{mm}$    | $\leq 4\text{mm}$                      | N/A                | $\leq 2$ , The accuracy would improve with added dwell positions and multiple scintillators.   |
| Optical Transparency            | 0.7                  | 0.78                                   | 0.72               | Multiple scintillators have an optical transparency $\geq 0.8$ , however, no publications state a minimum requirement.   |
| Fibre diameter                  | $\leq 0.3\text{mm}$  | 0.5mm                                  | 0.2mm              | 0.2mm  |
| Radiation hardness of the fibre | 6 Months             | N/A                                    | N/A                | The Optran®Ultra WFGE fibre. The PMMA fibre is not sufficient to withstand the radiation for 6 months. (10)  |
| Temperature dependency          | 10-50°C              | 22-24°C (42)                           | 20°C               | ZnSe: O(39)  |

Table 8.1: Validation of the optical performance

### 8.0.2. Validation of the current literature

This report aimed to give Elekta advice on the coupling and fibre diameter of a new OIVD sensor assembly to evaluate the dose delivery for brachytherapy (BT). As source placement errors can affect the effectiveness of the treatment, dose verification is desired. With real-time feedback of the dose delivered to the planning target volume (PTV) and the organ at risks (OARs), the oncologist can ensure the accuracy and conformality of the dose delivery. This will improve patient outcomes after treatment.

#### 1. Most suitable scintillator

The literature study shows that multiple scintillators will sufficiently excite characteristic light as a response to the  $^{192}\text{Ir}$  isotope. Ruby ( $\text{Al}_2\text{O}_3 : \text{C}$ ) is widely available and therefore mentioned in a lot of experimental papers. However, when we look into the ideal characteristics  $\text{ZnSe} : \text{O}$  looks most promising and is widely available. On top of that, more scintillators are likely available soon at an affordable cost.

#### 2. Most efficient coupling

To my knowledge, it is still unknown what the minimum amount of light signal needs to reach the photodetector to accurate dose measurement. More recently, different coupling methods have been introduced to the development of OIVD sensor systems to increase the light throughput. Mathematical models assume that optical antennas (tapered optical fibres) and lenses will increase the coupling efficiency. However, there are very limited prototypes tested to verify the mathematical models. The reduced volume of the scintillator will lower the total amount of generated photons, and it is unknown if the coupling efficiency will compensate for the loss.

#### 3. Uncertainties during dose measurement

Analyzing the uncertainties used in clinical dosimetry is critical to getting accurate results. Multiple papers state that concern in BT is a lack of knowledge about the frequency and nature of errors and the amount of Cherenkov radiation produced in the scintillator.



# 9

## Conclusion

This study aimed to overview the requirements for the sensing part of an optical IVD sensor assembly to couple light efficiently into an optical fibre. This is done by coupling the smallest fibre diameter and most basic coupling design for an optical optical *in vivo* dosimetry (OIVD) sensor assembly to be able to obtain sufficient light yield, given the HDR brachytherapy application, the selected fibre and the available scintillator dimensions and materials.

Experimental data for finding the most suitable scintillators that fit in the head of an OIVD sensor system and the different coupling approaches to couple the produced light into an optical fibre of  $100\text{-}300\mu\text{m}$ , was available from earlier research. This helped to answer the main research question, using seven COMSOL Multiphysics (CM) models. During this project, simulation data from CM and literature became available. This was used to find the most suitable scintillators that fit in the head of an OIVD sensor system and the different coupling approaches couple the produced light into the optical fibre. The OIVD sensor assemblies have proven successful in detecting the  $^{192}\text{Ir}$  isotope (6).

From all these models, the inorganic scintillator  $\text{ZnSe}:\text{O}$  has favourable scintillation characteristics and is helpful in a device for radiation therapy application with its high intensity and slight afterglow. Next to this, the sensor also demonstrates good repeatability, with a maximum error of 4.13% compared to the expected result from the treatment planning system calculation algorithm, TG43 (87). For good and efficient light transmission, the cross-sectional area and the numerical apertures (NA) need to be maximized (25).

OIVD sensor systems have the potential for dose verification for  $^{192}\text{Ir}$  brachytherapy (BT), this is demonstrated with the simulations. These show that the  $\text{ZnSe}:\text{O}$  has the best optical performance. An optical fibre between  $200\text{-}250\mu\text{m}$  will be large enough to have a sufficient light yield at the detector. The potential benefit will justify the use of *in vivo* dosimetry (IVD) once OIVD sensor assemblies are commercially available. Also, when IVD becomes mandatory in all countries to record the dose delivered to patients, the price of scintillators will likely decrease, and these sensor systems will become affordable.

A model of the head of an OIVD sensor assembly is simulated in COMSOL Multiphysics to characterise the model dimensions and their impact on the coupling efficiency. This then led to seven designs. All models were consistent with the theoretical expectations, with the sidenote that the material properties can be slightly different from the theory. Based on this report, it can be concluded that the head on an OIVD can couple the exited light into a fibre while minimising the light loss and maximising the coupling efficiency. This is done by encapsulating the ball coupled scintillator in the same stainless steel capsule as the  $^{192}\text{Ir}$  source.

The main conclusion drawn in this thesis is that with the current implementation of models, the fibre diameter can be reduced to  $200\mu\text{m}$ , which is feasible to fit the OIVD sensor assembly in the transfer tubes and needles.





# 10

## Recommendations

Due to the limited amount of time and the complexity of the optical *in vivo* dosimetry (OIVD) sensor system, it is not possible to incorporate every aspect in this graduation thesis. This also applies to all imperfections of the COMSOL model, that couldn't be erased and corrected to come to the final design. To compensate, a recommendation for future projects is to implement the OIVD sensor system in the clinic. In the chapter, the proposal for improvements of this project is handled in section 10.1. For continuation or improving this project, suggestions are given for manufacturing in section 10.2 and concluded with recommendations for testing in section 10.3.

### 10.1. Improvements of the COMSOL model

The discussion points for modelling the COMSOL Multiphysics (CM) model are listed below:

1. The OIVD model is rather simple in this design. to improve the reliability of the model, some extra things could be implemented:
  - (a) The actual materials can be implemented with real-life dopants and impurities. However, this comes with additional losses and a higher computational power.
  - (b) The scintillator won't release the rays in a perfectly rectangular grid and with constant power output but is based on the distance to the source, the age of the source and the quality of the scintillator. But before this can be implemented, more research is needed to get a better understanding of the scintillation behaviour in the head of a OIVD sensor system.

These effects likely need to be verified through testing, but they can be better predicted if these aspects are implemented first. On top of that, it can give a more complete answer to the sub-question:

    - (i) Which scintillation requirements are needed for a scintillator to detect the presence of an  $^{192}\text{Ir}$  source at a 2.5-150 mm distance?
2. The design can be improved by implementing the coating around the scintillator. By replacing the boundary with extra material come with a computational cost but will improve the quality of the solution. Also, adjusting the roughness of the boundaries might increase the coupling efficiency. Changing the smoothness of the scintillator or implementing a pattern will increase the efficiency of the OIVD sensor system. When the CM model has recreated overusing this model, changing these parts should be taken into account.
3. During this project, it became clear that the ray optics module users guide is not complete (18). This makes working in this model extra hard for a new user, one of the major drawbacks was not being able to use the ray detector node to analyse the rays in the model. This would give insights into the influence of the individual ray scattering, reflection, and absorption. Although the final results could be acquired in CM with a rather long computation time, exporting the data to MATLAB gave no additional value to a meshing error. Next to this, not being able to export the data makes it impossible to generate comparative plots, and therefore only a limited amount of results could be obtained.

4. To limit the computational time, the model is created in a 2D workspace. This could be done because the model is axisymmetrical. However, analysing the model in 3D would give more insight into how rays would enter the fibre and the distribution of the rays. Having a good understanding of the ray distribution provides the user with more insight in improving the geometrical shape of the OIVD sensor assembly.
5. To improve the performance, a multiphysics interaction can be made in CM, so the strength of the enhancement can be taken into account as well as the influence of heat coming from the human body. These interactions will improve the model and let analyses will be more truthful.
6. The data processing in CM is not always clear, and some actions need to be taken to improve the post-process of the acquired data. It is possible to extract a MATLAB scripts from COMSOL. Nonetheless, these scripts are very unclear and need to be improved to increase the useability and reduce the manual effort:
  - (a) The exported data from COMSOL is in a hard to read format: Some options for output are not available, e.g. parameters for columns. Next to this, some of the physics equations and how they are used can't be opened, so the user cannot verify the data. For a faster post-processing routine, improving the format of the different data files is key.
  - (b) Currently, the data in COMSOL are stored as global or ray parameters. These parameters can work together while influencing each other. Easy interaction between these data types will help the user to acquire more reliable data from the software.
  - (c) Generating plots and legends in CM all needs to be done manually. To generate the plot files, plot files and axis automatically, the post-processing time will be reduced.

Although the current simulation of the OIVD model works when appropriately used, to make it more reliable and user-friendly, improving these steps will improve new users to extract meaningful data with less effort.

## 10.2. Fabrication of the OIVD sensor system

When the project started, the fabrication of a scale model for the OIVD was intended. But as the project continued, it was rejected from the research scope. In this section, multiple suggestions are given for a continuation of the development of a OIVD sensor system. During the project, numerous models and sketches are made and implemented in CM. Below a global process is given based on the findings from the literature as described in chapter 3 and chapter 4 as well as the final COMSOL results given in chapter 7

1. To obtain a high light yield with an exiting wavelength distinguished from the wavelength of the Cerenkov radiation, the OIVD sensor assembly should be built around the inorganic scintillator *ZnSe:OI*.
2. The use of a ball antenna inside the OIVD will improve the coupling efficiency at a relatively low cost.
3. The CM models show that the adding a reflective coating around the scintillator, the light coupling efficiency will increase significantly.
4. The PMMA fibre used in the CM model had a low coupling efficiency, so using the Ge-doped fused Silica-doped fibre by CeramOptec will probably lead to better performance.
5. There are multiple ways to connect the scintillator to the optical fibre, but no research is done to increase the coupling efficiency that way. With the literature in mind, a tapered fibre will probably suit best.
6. The absorption in the protective capsule of the scintillator is not taken into account. Research is needed to acquire a better material and structure to increase the light yield of the scintillation crystal.

Note that there is an option to vary the total volume of the space in the capsule a bit more than in chapter 6. And implementing additional background fibre and reflective measurements will influence the coupling efficiency, but it is outside of the scope of this research.

### 10.3. *in-vitro* and *in-vivo* testing of the OIVD model

Although the device configuration isn't finalised and the testing results highly depend on this, a testing method for the OIVD sensor assembly is suggested in this chapter. With *in-vitro* test, it's possible to verify the simulations executed in CM and determine the reliability of the software. With these tests, the following questions can be answered:

1. How to maximise the number of ejected detectable photons in a scintillator?
2. How to realise the most efficient light coupling, give the maximum dimension of the |glsivd sensor assembly?
3. Is the light transport in an experimental setup similar to the model?
4. What is the minimum required signal to verify the dose delivered?
5. Are there more issues that arise in an experimental setup that is not mentioned in other literature and not taken into account in the current CM model?

These five questions can be answered in an experimental setup using the following items:

- (i) Use an active source that can move along the OIVD sensor assembly. Multiple sources can be used to meet the ALARA principles, but an  $^{192}$  is desired.
- (ii) Use a photodiode to measure the amount of light reaching the end of the optical fibre, so it is known how much light is needed to accurately measure the delivered dose and determine if a photomultiplier tube is required.
- (iii) Use a background fibre to determine if the stem effect is dominant in the signal and to define it needs to be filtered out.

Using the knowledge presented in this report will provide guidelines for a potential device testing setup.



# Bibliography

- [1] Robert Abbe. The use of radium in malignant disease. *The Lancet*, 182(4695):524–527, 1913.
- [2] Sadao Adachi and Tsunemasa Taguchi. Optical properties of znse. *Physical review B*, 43(12):9569, 1991.
- [3] Mikhail S Alekhin, Johan TM de Haas, Karl W Kramer, and Pieter Dorenbos. Scintillation properties. *IEEE transactions on nuclear science*, 58(5):2519–2527, 2011.
- [4] Mikhail Sergeevich Alekhin. New halide scintillators for gamma ray detection. *repository.tudelft.nl*, 2013.
- [5] Claus E Andersen, Soren Kynde Nielsen, Steffen Greulich, Jakob Helt-Hansen, Jacob Christian Lindegaard, and Kari Tanderup. Characterization of a fiber-coupled luminescence dosimetry system for online in vivo dose verification during brachytherapy. *Medical physics*, 36(3):708–718, 2009.
- [6] Claus E Andersen, Søren Kynde Nielsen, Jacob Christian Lindegaard, and Kari Tanderup. Time-resolved in vivo luminescence dosimetry for online error detection in pulsed dose-rate brachytherapy. *Medical physics*, 36(11):5033–5043, 2009.
- [7] Louis Archambault, A Sam Beddar, Luc Gingras, René Roy, and Luc Beaulieu. Measurement accuracy and cerenkov removal for high performance, high spatial resolution scintillation dosimetry. *Medical physics*, 33(1):128–135, 2006.
- [8] S Baccaro, K Blazek, and De Notaristefani. Scintillation properties of yap:ce. *Nuclear Instruments and Methods in Physics Research Section A: Accelerators, Spectrometers, Detectors and Associated Equipment*, 361(1-2):209–215, 1995.
- [9] A Sam Beddar, Susan Law, Natalka Suchowerska, and T Rockwell Mackie. Plastic scintillation dosimetry: optimization of light collection efficiency. *Physics in Medicine & Biology*, 48(9):1141, 2003.
- [10] Sam Beddar and Luc Beaulieu. *Scintillation dosimetry*. CRC Press, 2016.
- [11] S Belogurov, G Bressi, G Carugno, E Conti, D Iannuzzi, and A.T Meneguzzo. Csi(tl) infrared scintillation light yield and spectrum. *Nuclear Instruments and Methods in Physics Research Section A: Accelerators, Spectrometers, Detectors and Associated Equipment*, 449(1):254–259, 2000.
- [12] Gregory Bizarri, Edith D Bourret-Courchesne, Zewu Yan, and Steve E Derenzo. Scintillation and optical properties. *IEEE Transactions on Nuclear Science*, 58(6):3403–3410, 2011.
- [13] Lars Bøtter-Jensen, Stephen WS McKeever, and Ann G Wintle. *Optically stimulated luminescence dosimetry*. Elsevier, 2003.
- [14] Paul Brinckmann. Csi (na) scintillation crystals. *Phys. Letters*, 15, 1965.
- [15] Albertus Sybrandus Keverling Buisman. *Handboek radionucliden*. Uitgeverij Nucleus, 2015.
- [16] Mauro Carrara, Claudia Cavatorta, Marta Borroni, Chiara Tenconi, Annamaria Cerrotta, Carlo Fallai, Grazia Gambarini, Anna Vedda, and Emanuele Pignoli. Characterization of a ce3+ doped sio2 optical dosimeter for dose measurements in hdr brachytherapy. *Radiation measurements*, 56:312–315, 2013.
- [17] Abdulhamid Chaikh, Arnaud Gaudu, and Jacques Balosso. Monitoring methods for skin dose in interventional radiology. *International Journal of Cancer Therapy and Oncology*, 3(1):03011, 2014.
- [18] COMSOL. Ray optics module users guide, Accessed: 01-03-2020. <https://doc.comsol.com/5.5/doc/com.comsol.help.roptics/RayOpticsModuleUsersGuide.pdf>.
- [19] J Adam Martin Cunha, Ryan Flynn, Cédric Bélanger, Cameron Callaghan, Yusung Kim, Xun Jia, Zhe Chen, and Luc Beaulieu. Brachytherapy future directions. In *Seminars in radiation oncology*, volume 30, pages 94–106. Elsevier, 2020.

- [20] Liang Ding, Qiong Wu, Qun Wang, Yamei Li, Richard M Perks, and Liang Zhao. Advances on inorganic scintillator-based optic fiber dosimeters. *EJNMMI physics*, 7(1):1–23, 2020.
- [21] P Dorenbos, J Th M de Haas, and CWE Van Eijk. Non-proportionality in the scintillation response and the energy resolution obtainable with scintillation crystals. *IEEE Transactions on Nuclear Science*, 42(6):2190–2202, 1995.
- [22] Pieter Dorenbos. Fundamental limitations in the performance of activated scintillators. *IEEE Transactions on Nuclear Science*, 57(3):1162–1167, 2010.
- [23] Mildred Dresselhaus, Gene Dresselhaus, Stephen B Cronin, and A Gomes Souza Filho. *Solid State Properties*. Springer, 2018.
- [24] Winicjusz Drozdowski, Andrzej J Wojtowicz, Tadeusz Lukasiewicz, and Jaros law Kisielewski. Scintillation properties of luap and luyap crystals activated with cerium and molybdenum. *Nuclear Instruments and Methods in Physics Research Section A: Accelerators, Spectrometers, Detectors and Associated Equipment*, 562(1):254–261, 2006.
- [25] Justin Elsey, David R McKenzie, Jamil Lambert, Natalka Suchowerska, Sue L Law, and Simon C Fleming. Optimal coupling of light from a cylindrical scintillator into an optical fiber. *Applied optics*, 46(3):397–404, 2007.
- [26] Public Health England. Safer radiotherapy: Supplementary data analysis, 2019.
- [27] I.K.K Kolkman-Deurloo Erasmus Medical Centre. Future perspectives for brachytherapy, May 2020.
- [28] Thomas G Flohr, Joseph Y Lo, and Taly Gilat Schmidt. Medical imaging 2017: Physics of medical imaging. In *SPIE*, volume 10132, 2017.
- [29] JM Fontbonne, G Iltis, Get al Ban, A Battala, JC Vernhes, J Tillier, NCLB Bellaize, C Le Brun, B Tamain, K Mercier, et al. Scintillating fiber dosimeter for radiation therapy accelerator. *IEEE Transactions on Nuclear Science*, 49(5):2223–2227, 2002.
- [30] Milton Furst and Hartmut Kallman. High energy induced fluorescence in organic liquid solutions (energy transport in liquids). iii. *Physical Review*, 85(5):816, 1952.
- [31] Ruby K Gill, Gregory S Mitchell, and Simon R Cherry. Computed cerenkov luminescence yields for radionuclides used in biology and medicine. *Physics in Medicine & Biology*, 60(11):4263, 2015.
- [32] David Goff. *Fiber optic reference guide*. CRC Press, 2002.
- [33] David J. Griffiths. *Introduction to Quantum Mechanics (2nd Edition)*. Pearson Prentice Hall, 2nd edition, April 2004.
- [34] Hamdan Hadi Kusuma, Budi Astuti, and Z. Ibrahim. Absorption and emission properties of rubysingle crystal. *Journal of Physics: Conference Series*, 1170:012054, 03 2019.
- [35] Brian Henderson and G Frank Imbusch. *Optical spectroscopy of inorganic solids*, volume 44. Oxford University Press, 2006.
- [36] Robert Hofstadter. Alkali halide scintillation counters. *Physical Review*, 74(1):100, 1948.
- [37] Peter Hoskin and Catherine Coyle. *Radiotherapy in practice-brachytherapy*. Oxford University Press, 2011.
- [38] ICRP. *ICRP Publication 86: Prevention of Accidents to Patients Undergoing Radiation Therapy*, volume 86. Elsevier Health Sciences, 2001.
- [39] ISMA. Znse(o), Accessed: 05-04-2021. <http://www.isma.kharkov.ua/en/node/31>.
- [40] Gerald Earle Jellison Jr, Lynn A Boatner, Joanne Oxendine Ramey, James A Kolopus, Lucas A Ramey, and David J Singh. Refractive index of sodium iodide. *Journal of Applied Physics*, 111(4):043521, 2012.

- [41] Jacob Johansen, Erik B Jørgensen, Susanne Rylander, Simon Buus, Lise Bentzen, Christian S. Søndergaard, Anders K. M. With, Gustavo Kertzscher, and Kari Tanderup. [oa084] source tracking with in vivo dosimetry for brachytherapy. *Physica Medica*, 52:33, 2018. Abstracts from the 2nd European Congress of Medical Physics.
- [42] Erik B Jørgensen, Gustavo Kertzscher, Simon Buus, Lise Bentzen, Steffen B Hokland, Susanne Rylander, Kari Tanderup, and Jacob G Johansen. Accuracy of an in vivo dosimetry-based source tracking method for afterloading brachytherapy—a phantom study. *Medical Physics*, 48(5):2614–2623, 2021.
- [43] Vaiva Kaveckyte. *Development of Experimental Brachytherapy Dosimetry Using Monte Carlo Simulations for Detector Characterization*. PhD thesis, Linköping University Electronic Press, 2021.
- [44] Gustavo Kertzscher, Claus E Andersen, Frank-André Siebert, Søren Kynde Nielsen, Jacob C Lindegaard, and Kari Tanderup. Identifying afterloading pdr and hdr brachytherapy errors using real-time fiber-coupled al<sub>2</sub>o<sub>3</sub>: C dosimetry and a novel statistical error decision criterion. *Radiotherapy and oncology*, 100(3):456–462, 2011.
- [45] Gustavo Kertzscher, Claus E Andersen, and Kari Tanderup. Adaptive error detection for hdr/pdr brachytherapy: Guidance for decision making during real-time in vivo point dosimetry. *Medical physics*, 41(5):052102, 2014.
- [46] Gustavo Kertzscher and Sam Beddar. Ruby-based inorganic scintillation detectors for 192ir brachytherapy. *Physics in Medicine & Biology*, 61(21):7744, 2016.
- [47] Gustavo Kertzscher and Sam Beddar. Inorganic scintillation detectors for 192ir brachytherapy. *Physics in Medicine & Biology*, 64(22):225018, 2019.
- [48] IV Khodyuk. Nonproportionality of inorganic scintillators. *repository.tudelft.nl*, 2013.
- [49] Ivan V Khodyuk, Johan TM de Haas, and Pieter Dorenbos. Nonproportional response between 0.1–100 keV energy by means of highly monochromatic synchrotron x-rays. *IEEE Transactions on Nuclear Science*, 57(3):1175–1181, 2010.
- [50] Glenn F Knoll. *Radiation detection and measurement*. John Wiley & Sons, 2010.
- [51] Paul Lecoq, Alexander Annenkov, Alexander Gektin, Mikhail Korzhik, and Christian Pedrini. Scintillation and inorganic scintillators. *Inorganic Scintillators for Detector Systems: Physical Principles and Crystal Engineering*, pages 1–34, 2006.
- [52] William R Leo. *Techniques for nuclear and particle physics experiments: a how-to approach*. Springer Science & Business Media, 2012.
- [53] H. Malitson and M. J. Dodge. Refractive index and birefringence of synthetic sapphire. *Handbook of Laser Science and Technology*, IV:30, 1986.
- [54] M Malvezzi, G Carioli, P Bertuccio, P Boffetta, F Levi, C La Vecchia, and E Negri. European cancer mortality predictions for the year 2019 with focus on breast cancer. *Annals of Oncology*, 30(5):781–787, 2019.
- [55] Nahuel Martinez, Tobias Teichmann, Pablo Molina, Marian Sommer, Martin Santiago, Jürgen Henniger, and Eduardo Caselli. Scintillation properties of the yvo<sub>4</sub>: Eu<sup>3+</sup> compound in powder form: its application to dosimetry in radiation fields produced by pulsed mega-voltage photon beams. *Zeitschrift fuer Medizinische Physik*, 25(4):368–374, 2015.
- [56] Robert J Moon. Inorganic crystals for the detection of high energy particles and quanta. *Physical Review*, 73(10):1210, 1948.
- [57] Angel Morales-Ramirez, Antonieta García Murillo, Felipe Carrillo-Romo, García-Hernández Margarita, Elder De la Rosa, and Joel Palmerin. Y<sub>2</sub>O<sub>3</sub>:eu<sup>3+</sup>,tb<sup>3+</sup> thin films prepared by sol-gel method: Structural and optical studies. *Journal of Sol-Gel Science and Technology*, 58:366–373, 05 2011.
- [58] WW Moses, GA Bizarri, Richard Taylor Williams, SA Payne, AN Vasil’Ev, J Singh, Q Li, JQ Grim, and W-S Choong. The origins of scintillator non-proportionality. *IEEE Transactions on Nuclear Science*, 59(5):2038–2044, 2012.

- [59] M Moszynski, T Ludziejewski, D Wolski, W Klamra, and LO Norlin. Properties of the yag: Ce scintillator. *Nuclear Instruments and Methods in Physics Research Section A: Accelerators, Spectrometers, Detectors and Associated Equipment*, 345(3):461–467, 1994.
- [60] Yutaka Nigara. Measurement of the optical constants of yttrium oxide. *Japanese Journal of Applied Physics*, 7(4):404, 1968.
- [61] EDMUND OPTICS. Preloaded norland optical adhesive syringes, Accessed: 12-10-2021. <https://www.edmundoptics.com/f/preloaded-norland-optical-adhesive-syringes/39757/>.
- [62] P Ortiz and M Wheatley. Lessons learned from accidental exposures in radiotherapy. *IAEA Safety Reports Series*, 17:59–61, 2000.
- [63] C Pedrini. Scintillation mechanisms and limiting factors on each step of relaxation of electronic excitations. *Physics of the Solid State*, 47(8):1406–1411, 2005.
- [64] 2004-2016 Saint-Gobain Ceramics & Plastics. Nai(tl) scintillation crystals, Accessed: 02-03-2021. [https://www.crystals.saint-gobain.com/sites/imdf.crystals.com/files/documents/yag-material-data-sheet\\_69775.pdf](https://www.crystals.saint-gobain.com/sites/imdf.crystals.com/files/documents/yag-material-data-sheet_69775.pdf).
- [65] 2004-2016 Saint-Gobain Ceramics & Plastics. Csi(tl) thallium activated cesium iodide, Accessed: 1-01-2021. [https://www.crystals.saint-gobain.com/sites/imdf.crystals.com/files/documents/yag-material-data-sheet\\_69775.pdf](https://www.crystals.saint-gobain.com/sites/imdf.crystals.com/files/documents/yag-material-data-sheet_69775.pdf).
- [66] 2004-2016 Saint-Gobain Ceramics & Plastics. Lyso scintillation material, Accessed: 12-12-2020. <https://www.crystals.saint-gobain.com/sites/imdf.crystals.com/files/documents/lyso-material-data-sheet.pdf>.
- [67] 2004-2016 Saint-Gobain Ceramics & Plastics. Yag(ce) yttrium aluminum garnet scintillation material, Accessed: 5-11-2020. [https://www.crystals.saint-gobain.com/sites/imdf.crystals.com/files/documents/yag-material-data-sheet\\_69775.pdf](https://www.crystals.saint-gobain.com/sites/imdf.crystals.com/files/documents/yag-material-data-sheet_69775.pdf).
- [68] Jerry L Prince and Jonathan M Links. *Medical imaging signals and systems*. Pearson Prentice Hall Upper Saddle River, 2006.
- [69] Mark J Rivard, Bert M Coursey, Larry A DeWerd, William F Hanson, M Saiful Huq, Geoffrey S Ibbott, Michael G Mitch, Ravinder Nath, and Jeffrey F Williamson. Update of aapm task group no. 43 report: A revised aapm protocol for brachytherapy dose calculations. *Medical physics*, 31(3):633–674, 2004.
- [70] PA Rodnyi, P Dorenbos, and CWE Van Eijk. Energy loss in inorganic scintillators. *physica status solidi (b)*, 187(1):15–29, 1995.
- [71] Piotr A Rodnyi. *Physical processes in inorganic scintillators*, volume 14. CRC press, 1997.
- [72] ROBERT J Shalek and MARILYN Stovall. Brachytherapy dosimetry. *The dosimetry of ionizing radiation*, 3:259–321, 1990.
- [73] Navid Soltani and Mario Agio. Planar antenna designs for efficient coupling between a single emitter and an optical fiber. *Optics express*, 27(21):30830–30841, 2019.
- [74] Ian N Stanton, Matthew D Belley, Giao Nguyen, Anna Rodrigues, Yifan Li, David G Kirsch, Terry T Yoshizumi, and Michael J Therien. Europium-and lithium-doped yttrium oxide nanocrystals that provide a linear emissive response with x-ray radiation exposure. *Nanoscale*, 6(10):5284–5288, 2014.
- [75] Miguel Angel Suarez, Tony Lim, Louise Robillot, Valentin Maillot, Thomas Lihoreau, Patrick Bontemps, Lionel Pazart, and Thierry Grosjean. Miniaturized fiber dosimeter of medical ionizing radiations on a narrow optical fiber. *Optics express*, 27(24):35588–35599, 2019.
- [76] Kenneth S Suslick. Encyclopedia of physical science and technology. *Sonoluminescence and sonochemistry*, 3rd edn. Elsevier Science Ltd, Massachusetts, pages 1–20, 2001.



- [77] Nancy Swanson and Mirosław Jonasz. Attenuation of light: Contributing processes. *Top. Part. Disp. Sci., Online Journal*, 11 2007.
- [78] Ashutosh Tewari. *Prostate cancer: A comprehensive perspective*. Springer Science & Business Media, 2013.
- [79] Hannah Tharmalingam, Yatman Tsang, Ananya Choudhury, Roberto Alonzi, James Wylie, Imtiaz Ahmed, Ann Henry, Catherine Heath, and Peter J Hoskin. External beam radiation therapy (ebrt) and high-dose-rate (hdr) brachytherapy for intermediate and high-risk prostate cancer: The impact of ebrt volume. *International Journal of Radiation Oncology\* Biology\* Physics*, 106(3):525–533, 2020.
- [80] Francois Therriault-Proulx, Sam Beddar, Tina M Briere, Louis Archambault, and Luc Beaulieu. Removing the stem effect when performing ir-192 hdr brachytherapy in vivo dosimetry using plastic scintillation detectors: A relevant and necessary step. *Medical physics*, 38(4):2176–2179, 2011.
- [81] Francois Therriault-Proulx, Tina M Briere, Firas Mourtada, Sylviane Aubin, Sam Beddar, and Luc Beaulieu. A phantom study of an in vivo dosimetry system using plastic scintillation detectors for real-time verification of 192ir hdr brachytherapy. *Medical physics*, 38(5):2542–2551, 2011.
- [82] Niluja Thiruthaneeswaran, Nicki Groom, Gerry Lowe, Linda Bryant, and Peter J Hoskin. Focal boost to residual gross tumor volume in brachytherapy for cervical cancer—a feasibility study. *Brachytherapy*, 17(1):181–186, 2018.
- [83] T. A. Callcott U. S. Whang, E. T. Arakawa. Optical properties of cs for photons of energy. *Optical*, pages 740–745, 1971.
- [84] Jack Valentin. Prevention of high-dose-rate brachytherapy accidents. icrp publication 97. *Annals of the ICRP*, 35(2):1–51, 2005.
- [85] EVD Van Loef, P Dorenbos, CWE Van Eijk, Karl Kramer, and Hans-Ulrich Gudel. High-energy-resolution scintillator: Ce 3+ activated labr 3. *Applied physics letters*, 79(10):1573–1575, 2001.
- [86] Javier Vijande, Domingo Granero, Jose Perez-Calatayud, and Facundo Ballester. Monte carlo dosimetric study of the flexisource co-60 high dose rate source. *Journal of contemporary brachytherapy*, 4(1):34, 2012.
- [87] P. Woulfe, F. J. Sullivan, W. Kam, and S. O’Keeffe. Optical fiber dosimeter for real-time in-vivo dose monitoring during ldr brachytherapy. *Biomed. Opt. Express*, 11(7):4027–4036, Jul 2020.
- [88] Yuntao Wu, Guohao Ren, Martin Nikl, Xiaofeng Chen, Dongzhou Ding, Huanyin Li, Shangke Pan, and Fan Yang. Csi: Tl+, yb 2+: ultra-high light yield scintillator with reduced afterglow. *CrystEngComm*, 16(16):3312–3317, 2014.
- [89] Yasuo Yoshioka, Jun Itami, Masahiko Oguchi, and Takashi Nakano. *Brachytherapy: Techniques and Evidences*. Springer, 2018.
- [90] LCL Yuan and Chien-Shiung Wu. *Fundamental principles and methods of particle detection*, 1961.
- [91] Eduardo G Yukihiro and Stephen WS McKeever. *Optically stimulated luminescence: fundamentals and applications*. John Wiley & Sons, 2011.
- [92] Lina Zhao, Shouhao Zhou, Peter Balter, Chan Shen, Daniel R Gomez, James D Welsh, Steve H Lin, and Joe Y Chang. Planning target volume d95 and mean dose should be considered for optimal local control for stereotactic ablative radiation therapy. *International Journal of Radiation Oncology\* Biology\* Physics*, 95(4):1226–1235, 2016.
- [93] Yu Zorenko, K Fabisiak, and Zorenko. Comparative study of the luminescence of al2o3: C and al2o3 crystals under synchrotron radiation excitation. *Journal of luminescence*, 144:41–44, 2013.



# A

## Labels

|                                       |  |  |  |   |   |  |  |   |   |  |  |   |  |   |  |   |   |
|---------------------------------------|--|--|--|---|---|--|--|---|---|--|--|---|--|---|--|---|---|
| 1<br><b>H</b><br>HYDROGEN<br>1.0079   |  |  |  |   |   |  |  |   |   |  |  |   |  |   |  |   | 2<br><b>He</b><br>HELIUM<br>4.0026      |
| 3<br><b>Li</b><br>LITHIUM<br>6.941    | 4<br><b>Be</b><br>BERYLLIUM<br>9.0122  |  |  |   |   |  |  |   |   |  |  | 5<br><b>B</b><br>BORON<br>10.811        | 6<br><b>C</b><br>CARBON<br>12.011      | 7<br><b>N</b><br>NITROGEN<br>14.007       | 8<br><b>O</b><br>OXYGEN<br>15.999        | 9<br><b>F</b><br>FLUORINE<br>18.998     | 10<br><b>Ne</b><br>NEON<br>20.179       |
| 11<br><b>Na</b><br>SODIUM<br>22.989   | 12<br><b>Mg</b><br>MAGNESIUM<br>24.305 |  |  |   |   |  |  |   |   |  |  | 13<br><b>Al</b><br>ALUMINIUM<br>26.981  | 14<br><b>Si</b><br>SILICON<br>28.085   | 15<br><b>P</b><br>PHOSPHORUS<br>30.974    | 16<br><b>S</b><br>SULFUR<br>32.065       | 17<br><b>Cl</b><br>CHLORINE<br>35.453   | 18<br><b>Ar</b><br>ARGON<br>39.948      |
| 19<br><b>K</b><br>POTASSIUM<br>39.098 | 20<br><b>Ca</b><br>CALCIUM<br>40.078   | 21<br><b>Sc</b><br>SCANDIUM<br>44.955    | 22<br><b>Ti</b><br>TITANIUM<br>47.887  | 23<br><b>V</b><br>VANADIUM<br>50.9415     | 24<br><b>Cr</b><br>CHROMIUM<br>51.9961  | 25<br><b>Mn</b><br>MANGANESE<br>54.938 | 26<br><b>Fe</b><br>IRON<br>55.845      | 27<br><b>Co</b><br>COBALT<br>58.933     | 28<br><b>Ni</b><br>NICKEL<br>58.6934      | 29<br><b>Cu</b><br>COPPER<br>63.546      | 30<br><b>Zn</b><br>ZINC<br>65.38         | 31<br><b>Ga</b><br>GALLIUM<br>69.723    | 32<br><b>Ge</b><br>GERMANIUM<br>72.64  | 33<br><b>As</b><br>ARSENIC<br>74.921      | 34<br><b>Se</b><br>SELENIUM<br>78.971    | 35<br><b>Br</b><br>BROMINE<br>79.904    | 36<br><b>Kr</b><br>KRYPTON<br>83.798    |
| 37<br><b>Rb</b><br>RUBIDIUM<br>85.467 | 38<br><b>Sr</b><br>STRONTIUM<br>87.62  | 39<br><b>Y</b><br>YTRIUM<br>88.9058      | 40<br><b>Zr</b><br>ZIRCONIUM<br>91.224 | 41<br><b>Nb</b><br>NIOBIUM<br>92.9063     | 42<br><b>Mo</b><br>MOLYBDENUM<br>95.93  | 43<br><b>Tc</b><br>TECHNETIUM<br>(98)  | 44<br><b>Ru</b><br>RUTHENIUM<br>101.07 | 45<br><b>Rh</b><br>RHODIUM<br>102.90    | 46<br><b>Pd</b><br>PALLADIUM<br>106.42    | 47<br><b>Ag</b><br>SILVER<br>107.8682    | 48<br><b>Cd</b><br>CADMIUM<br>112.414    | 49<br><b>In</b><br>INDIUM<br>114.818    | 50<br><b>Sn</b><br>TIN<br>118.710      | 51<br><b>Sb</b><br>ANTIMONY<br>121.757    | 52<br><b>Te</b><br>TELLESIUM<br>127.60   | 53<br><b>I</b><br>IODINE<br>126.90      | 54<br><b>Xe</b><br>XEON<br>131.29       |
| 55<br><b>Cs</b><br>CAESIUM<br>132.905 | 56<br><b>Ba</b><br>BARIUM<br>137.327   | 57-71*<br>LANTHANIDE SERIES              | 72<br><b>Hf</b><br>HAFNIUM<br>178.49   | 73<br><b>Ta</b><br>TANTALUM<br>180.94     | 74<br><b>W</b><br>WOLFRAM<br>183.84     | 75<br><b>Re</b><br>RHENIUM<br>186.207  | 76<br><b>Os</b><br>OSMIUM<br>190.23    | 77<br><b>Ir</b><br>IRIDIUM<br>192.217   | 78<br><b>Pt</b><br>PLATINUM<br>195.084    | 79<br><b>Au</b><br>GOLD<br>196.9665      | 80<br><b>Hg</b><br>MERCURY<br>200.59     | 81<br><b>Tl</b><br>THALLIUM<br>204.38   | 82<br><b>Pb</b><br>LEAD<br>207.2       | 83<br><b>Bi</b><br>BISMUTH<br>208.98      | 84<br><b>Po</b><br>POLONIUM<br>(209)     | 85<br><b>At</b><br>ASTATINE<br>(210)    | 86<br><b>Rn</b><br>RADON<br>(222)       |
| 87<br><b>Fr</b><br>FRANCIUM<br>(223)  | 88<br><b>Ra</b><br>RADIUM<br>(226)     | 89-103**<br>ACTINIDE SERIES              | 104<br><b>Rf</b><br>RUFORMIUM<br>(261) | 105<br><b>Db</b><br>DUBNIUM<br>(262)      | 106<br><b>Sg</b><br>SEABORGIUM<br>(263) | 107<br><b>Bh</b><br>BOHRIUM<br>(264)   | 108<br><b>Hs</b><br>HASSIUM<br>(265)   | 109<br><b>Mt</b><br>MEITNERIUM<br>(266) | 110<br><b>Ds</b><br>DARMSTADTIUM<br>(267) | 111<br><b>Rg</b><br>ROENTGENIUM<br>(268) | 112<br><b>Cn</b><br>COCHINCHIUM<br>(269) | 113<br><b>Uut</b><br>UNUNTRIUM<br>(270) | 114<br><b>Fl</b><br>FLEROVIUM<br>(271) | 115<br><b>Uup</b><br>UNUNPENTIUM<br>(272) | 116<br><b>Lv</b><br>LIVERMORIUM<br>(273) | 117<br><b>Ts</b><br>TENNESSIUM<br>(274) | 118<br><b>Og</b><br>OGANESSIUM<br>(276) |
| Lanthanide Series                     |  | * 57<br><b>La</b><br>LANTHANUM<br>138.90 | 58<br><b>Ce</b><br>CELESIUM<br>140.12  | 59<br><b>Pr</b><br>PRASEODYMIUM<br>140.90 | 60<br><b>Nd</b><br>NEODYMIUM<br>144.24  | 61<br><b>Pm</b><br>PROMETHIUM<br>(145) | 62<br><b>Sm</b><br>SAMARIUM<br>150.36  | 63<br><b>Eu</b><br>EUROPIUM<br>151.964  | 64<br><b>Gd</b><br>GADOLINIUM<br>157.25   | 65<br><b>Tb</b><br>TERBIUM<br>158.92     | 66<br><b>Dy</b><br>DYSPROSIUM<br>162.50  | 67<br><b>Ho</b><br>HOLMIUM<br>164.93    | 68<br><b>Er</b><br>ERBIUM<br>167.259   | 69<br><b>Tm</b><br>THULIUM<br>168.93      | 70<br><b>Yb</b><br>Ytterbium<br>173.054  | 71<br><b>Lu</b><br>LUTETIUM<br>174.967  |   |
| Actinide Series                       |  | ** 89<br><b>Ac</b><br>ACTINIUM<br>(227)  | 90<br><b>Th</b><br>THORIUM<br>232.0377 | 91<br><b>Pa</b><br>Protactinium<br>231.03 | 92<br><b>U</b><br>URANIUM<br>238.02     | 93<br><b>Np</b><br>NEPTUNIUM<br>(237)  | 94<br><b>Pu</b><br>PLUTONIUM<br>(244)  | 95<br><b>Am</b><br>AMERICIUM<br>(243)   | 96<br><b>Cm</b><br>CURIUM<br>(247)        | 97<br><b>Bk</b><br>BERKELIUM<br>(247)    | 98<br><b>Cf</b><br>CALIFORNIUM<br>(251)  | 99<br><b>Es</b><br>EINSTEINIUM<br>(252) | 100<br><b>Fm</b><br>FERMIUM<br>(257)   | 101<br><b>Md</b><br>MEISENERIUM<br>(258)  | 102<br><b>No</b><br>NOBELIUM<br>(259)    | 103<br><b>Lr</b><br>LAWRENCIUM<br>(262) |   |

Figure A.1: Periodic Table of the Elements with the Lanthanides highlighted

| Scintillator   | Peak Emission (nm) | Light Yield ( $10^3$ ph MeV $^{-1}$ ) | Density (g cm $^{-3}$ ) | $Z_{eff}$ | Decay time (ns) | Energy Resolution at 662 keV (%) | Attenuation length at 511 keV (mm) | photoelectric effect at 511 keV (%) | Ref. |
|--|--------------------|---------------------------------------|-------------------------|-----------|-----------------|----------------------------------|------------------------------------|-------------------------------------|------|
| <i>NaI: Tl</i> <sup>a</sup>                            | 415                | 45                                    | 3.67                    | 51        | 230             | 6.5                              | 29                                 | 17                                  | [36] |
| <i>CsI: Na</i> <sup>a</sup>                            | 410                | 47                                    | 4.51                    | 54        | 630             | 7.4                              | 23                                 | 21                                  | [14] |
| <i>CsI: Tl</i> <sup>a</sup>                            | 540                | 64                                    | 4.51                    | 54        | 600 - 6500      | 4.3                              | 23                                 | 21                                  | [88] |
| <i>SrI<sub>2</sub>: Eu</i> <sup>a</sup>                | 435                | 93                                    | 4.6                     | 50.3      | 1200            | 2.7                              | N/A                                | N/A                                 | [3]  |
| <i>CsB<sub>a</sub>2I5: Eu</i>                          | 435                | 92-102                                | 4.8                     | N/A       | 159 - 1138      | 3.8                              | N/A                                | N/A                                 | [12] |
| <i>BaBrI: Eu</i>                                       | 435                | 96-108                                | 4.94                    | N/A       | 408 - 447       | 4.8                              | N/A                                | N/A                                 | [12] |
| <i>YAG: Ce</i> <sup>b</sup>                            | 550                | 30                                    | 4.57                    | 35        | 70              | 7.2                              | 15                                 | N/A                                 | [59] |
| <i>YAP: Ce</i>   | 365                | 21                                    | 5.5                     | 33.6      | 25              | 4.4                              | 26                                 | 4.9                                 | [8]  |
| <i>LuAP: Ce</i>  | 365                | 12                                    | 8.3                     | 65        | 25              | 4.9                              | 10.5                               | 30                                  | [24] |
| <i>LYSO: Ce</i>  | 420                | 33.2                                  | 7.1                     | N/A       | 36              | 8                                | 12                                 | N/A                                 | [66] |
| <i>LuBr<sub>3</sub>: Ce</i> <sup>a</sup>               | 360                | 73                                    | 5.07                    | 46.9      | 17              | 2.6                              | 22                                 | 13.1                                | [85] |
| <i>Y<sub>2</sub>O<sub>3</sub>: Eu, Li</i> <sup>c</sup> | 600                | 79                                    | 5.00                    | 7.5       | 2100            | 16                               | N/A                                | N/A                                 | [74] |
| <i>Al<sub>2</sub>O<sub>3</sub>: Cr</i>                 | 416                | 2.5                                   | 3.95                    | 10        | 33              | N/A                              | N/A                                | N/A                                 | [93] |
| <i>ZnSe: O</i> <sup>d</sup>                            | 595                | 30                                    | 5.27                    | 32        | 84              | 11.9                             | N/A                                | N/A                                 | [47] |

Table A.1: Physical characteristics of the scintillators

<sup>a</sup>Hygroscopic<sup>b</sup>Refractive index at peak emission n=1.82<sup>c</sup>Refractive index at peak emission n=1.94<sup>d</sup>Refractive index at peak emission n=2.66

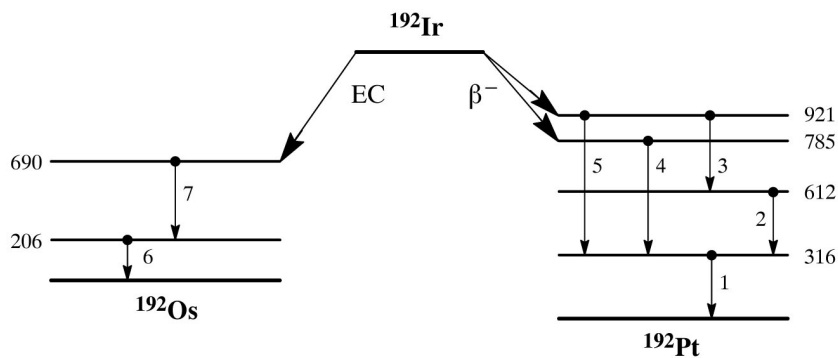
# B

Remaining results

**$^{192}\text{Ir}$**  **$Z = 77$** **Halveringstijd en vervalconstante**

$$T_{1/2} = 73,83 \text{ d} = 6,38 \times 10^6 \text{ s}$$

$$\lambda = 1,09 \times 10^{-7} \text{ s}^{-1}$$

**Vervalschema (vereenvoudigd)****Belangrijkste uitgezonden straling**

| Straling   | $y \text{ (Bq}\cdot\text{s)}^{-1}$ | $E \text{ (keV)}$ | Straling   | $y \text{ (Bq}\cdot\text{s)}^{-1}$ | $E \text{ (keV)}$ |
|------------|------------------------------------|-------------------|------------|------------------------------------|-------------------|
| $\beta^-$  | 0,415                              | 161   536         | $\gamma_4$ | 0,478                              | 468               |
| $\beta^-$  | 0,481                              | 209   672         | $\gamma_5$ | 0,082                              | 604               |
| $\gamma_1$ | 0,828                              | 316               | $\gamma_6$ | 0,033                              | 206               |
| $\gamma_2$ | 0,290                              | 296               | $\gamma_7$ | 0,032                              | 485               |
| $\gamma_3$ | 0,297                              | 308               |            |                                    |                   |

**Bronconstanten**

|                               |  |
|-------------------------------|--|
| Kermatempo in lucht           | $k = 0,11 \text{ } \mu\text{Gy/h per MBq/m}^2$ |
| Omgevingsdosisequivalenttempo | $h = 0,14 \text{ } \mu\text{Sv/h per MBq/m}^2$ |

**Diversen**

|                          |  |
|--------------------------|--|
| Specifieke activiteit    | $A_{\text{sp}} = 3,41 \times 10^{14} \text{ Bq/g}$             |
| Vrijstellingsgrenzen     | $C_v = 10^1 \text{ Bq/g}$ en $A_v = 10^4 \text{ Bq}$           |
| Huidbesmetting           | $H_{\text{huid}} = 5 \times 10^{-10} \text{ Sv/s per Bq/cm}^2$ |
| Wondbesmetting; Injectie | $e(50) = 7,0 \times 10^{-9} \text{ Sv/Bq}$                     |
| Vervoer                  | $A_1 = 1 \text{ TBq}$  |
|                          | $A_2 = 0,6 \text{ TBq}$  |

N = 115

 **$^{192}\text{Ir}$** **Productie en toepassingen**

Het radionuclide  $^{192}\text{Ir}$  is een activeringsproduct. Het wordt toegepast voor niet-destructief materiaalonderzoek. Bovendien vindt het toepassing als draad voor lokale bestralingen van tumoren.

**Metabool model**

Voor stralingshygiënische doeleinden wordt aangenomen dat iridium zich vanuit het bloed als volgt verdeelt: 20% naar lever, 4% naar nieren, 2% naar milt, 54% naar de overige organen/weefsels en de rest wordt rechtstreeks uitgescheiden. De biologische halveringstijd voor alle organen/weefsels wordt gesteld op: 20%  $T_{1/2} = 8 \text{ d}$  80%  $T_{1/2} = 200 \text{ d}$

**Ingestie- en longzuiveringsklassen**

Ingestie

Alle verbindingen  $f_1 = 0,01$ 

Inhalatie

|                             |              |          |
|-----------------------------|--------------|----------|
| Hydroxide, oxide            | $f_1 = 0,01$ | Klasse S |
| Halogenide, nitraat, metaal | $f_1 = 0,01$ | Klasse M |
| Overige verbindingen        | $f_1 = 0,01$ | Klasse F |

**Dosisconversiecoëfficiënt en radiotoxiciteitsequivalent voor werknemers (w) en voor leden van de bevolking (b)**

|             | Ingestie<br>$f_1 = 0,01$ | Inhalatie<br>F       | Inhalatie<br>M       | Inhalatie<br>S       |       |
|-------------|--------------------------|----------------------|----------------------|----------------------|-------|
| $e(50)(w)$  | $1,4 \times 10^{-9}$     | $2,2 \times 10^{-9}$ | $4,1 \times 10^{-9}$ | $4,9 \times 10^{-9}$ | Sv/Bq |
| $A_{Re}(w)$ | $7,1 \times 10^8$        | $4,5 \times 10^8$    | $2,4 \times 10^8$    | $2,0 \times 10^8$    | Bq    |
| $e(50)(b)$  | $1,4 \times 10^{-9}$     | $1,8 \times 10^{-9}$ | $4,9 \times 10^{-9}$ | $6,2 \times 10^{-9}$ | Sv/Bq |
| $A_{Re}(b)$ | $7,1 \times 10^8$        | $5,6 \times 10^8$    | $2,0 \times 10^8$    | $1,6 \times 10^8$    | Bq    |

**Gegevens voor totale-lichaamstelling**

| Tijd (d) | Lichaamsactiviteit na eenmalige inname (Bq per Bq inname) |                      |                      |                      |
|----------|---|----------------------|----------------------|----------------------|
| 0,25     | $9,9 \times 10^{-1}$                                      | $7,3 \times 10^{-1}$ | $7,4 \times 10^{-1}$ | $7,4 \times 10^{-1}$ |
| 1        | $7,1 \times 10^{-1}$                                      | $5,1 \times 10^{-1}$ | $4,9 \times 10^{-1}$ | $4,9 \times 10^{-1}$ |
| 2        | $3,3 \times 10^{-1}$                                      | $3,4 \times 10^{-1}$ | $2,5 \times 10^{-1}$ | $2,4 \times 10^{-1}$ |
| 3        | $1,3 \times 10^{-1}$                                      | $2,6 \times 10^{-1}$ | $1,5 \times 10^{-1}$ | $1,3 \times 10^{-1}$ |
| 5        | $2,5 \times 10^{-2}$                                      | $2,1 \times 10^{-1}$ | $8,5 \times 10^{-2}$ | $7,2 \times 10^{-2}$ |
| 7        | $9,1 \times 10^{-3}$                                      | $1,9 \times 10^{-1}$ | $7,4 \times 10^{-2}$ | $6,1 \times 10^{-2}$ |

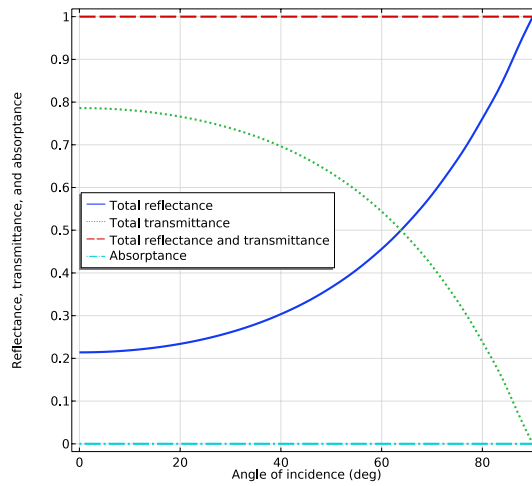
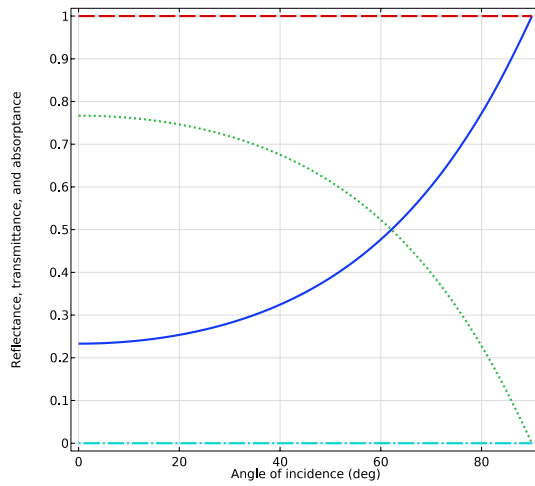
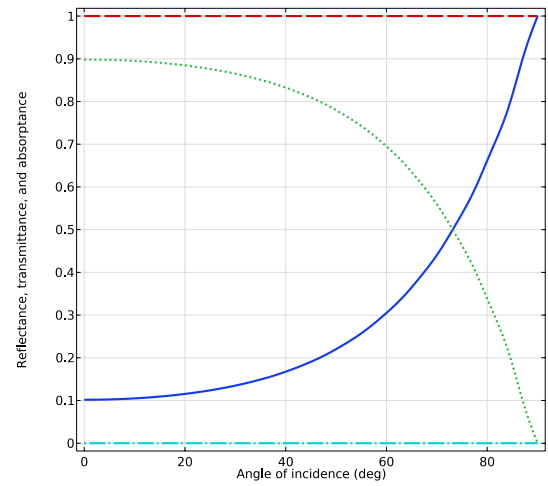
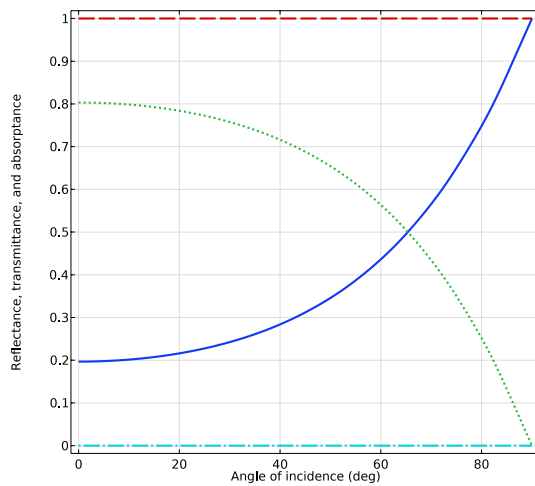
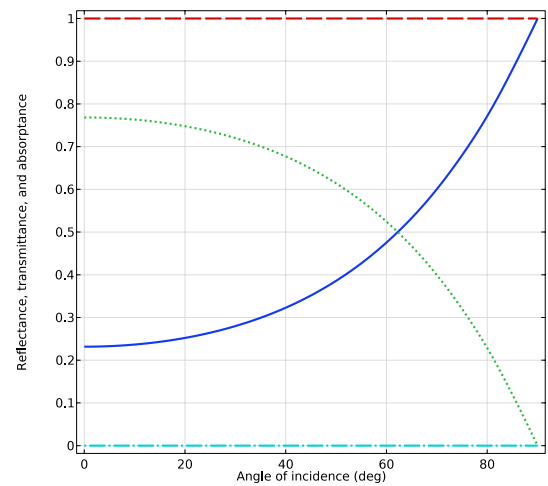
(a) NaI with  $\lambda=440$ (b) CsI with  $\lambda=540$ (c) ZnSe with  $\lambda=600$ (d)  $Y_2O_3$  with  $\lambda=610$ (e)  $Al_2O_3$  with  $\lambda=690$ 

Figure B.3: The behaviour of an incoming light ray at the material transition from scintillator to fibre without attenuation, executed in therapy-optics module in COMSOL Multiphysics



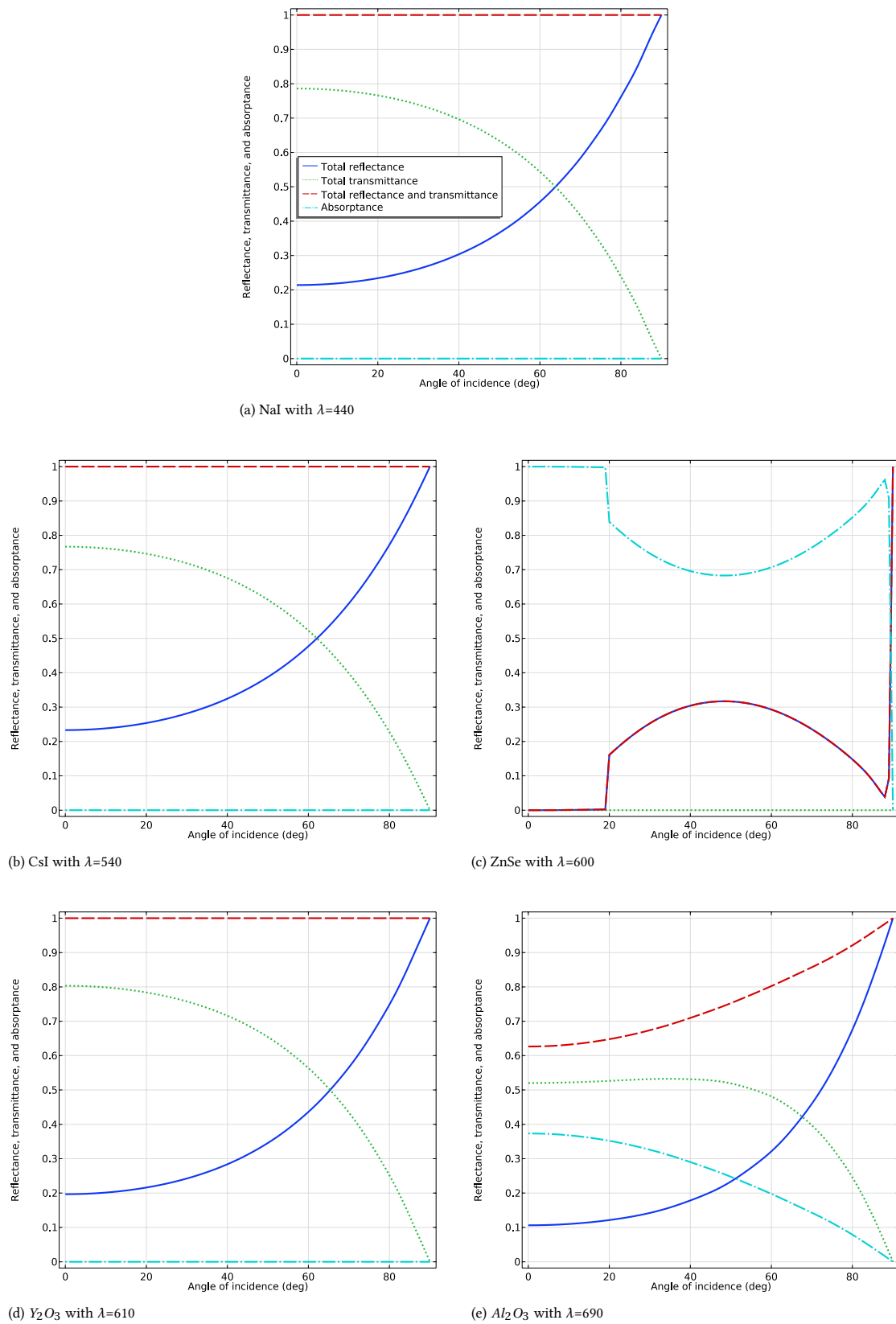


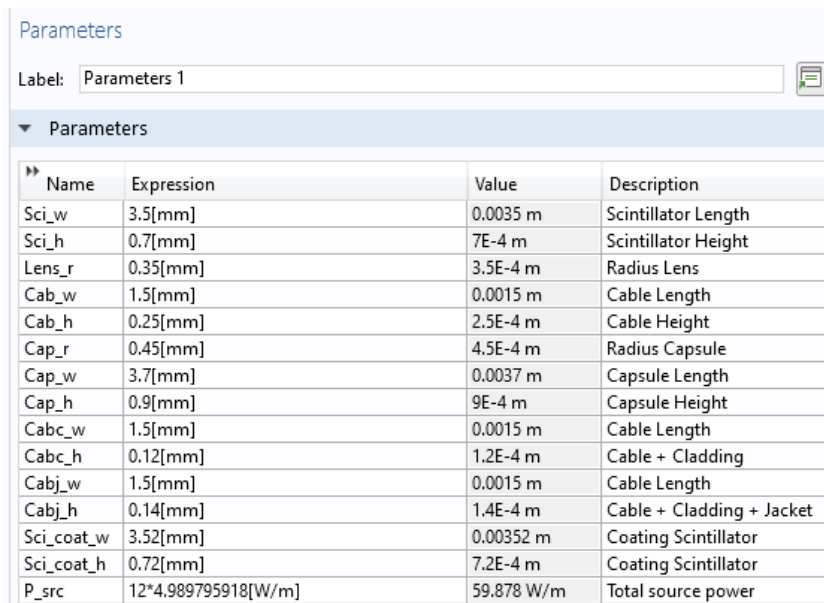
Figure B.4: The behaviour of an incoming light ray at the material transition from scintillator to fibre withattenuation, executed in therapy-optics module in COMSOL Multiphysics



# C

## COMSOL simulations

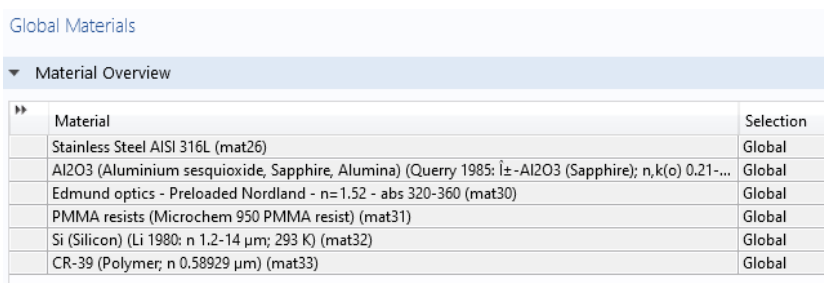
The modelling workflow in COMSOL Multiphysicsv5.5 is described here. This workflow consists of the following steps: 1. Setting up the model environment 2. Build the geometry for the optical in-vivo dosimetry sensor assembly 3. Import and specify the material properties 4. Defining the boundary conditions in the model. 5. Create the desired mesh. 6. Run the simulation 7. Postproces the results in COMSOL or other software.



The screenshot shows the 'Parameters' window in COMSOL Multiphysics. It contains a table with the following data:

| Name       | Expression          | Value      | Description               |
|------------|---------------------|------------|---------------------------|
| Sci_w      | 3.5[mm]             | 0.0035 m   | Scintillator Length       |
| Sci_h      | 0.7[mm]             | 7E-4 m     | Scintillator Height       |
| Lens_r     | 0.35[mm]            | 3.5E-4 m   | Radius Lens               |
| Cab_w      | 1.5[mm]             | 0.0015 m   | Cable Length              |
| Cab_h      | 0.25[mm]            | 2.5E-4 m   | Cable Height              |
| Cap_r      | 0.45[mm]            | 4.5E-4 m   | Radius Capsule            |
| Cap_w      | 3.7[mm]             | 0.0037 m   | Capsule Length            |
| Cap_h      | 0.9[mm]             | 9E-4 m     | Capsule Height            |
| Cabc_w     | 1.5[mm]             | 0.0015 m   | Cable Length              |
| Cabc_h     | 0.12[mm]            | 1.2E-4 m   | Cable + Cladding          |
| Cabj_w     | 1.5[mm]             | 0.0015 m   | Cable Length              |
| Cabj_h     | 0.14[mm]            | 1.4E-4 m   | Cable + Cladding + Jacket |
| Sci_coat_w | 3.52[mm]            | 0.00352 m  | Coating Scintillator      |
| Sci_coat_h | 0.72[mm]            | 7.2E-4 m   | Coating Scintillator      |
| P_src      | 12*4.989795918[W/m] | 59.878 W/m | Total source power        |

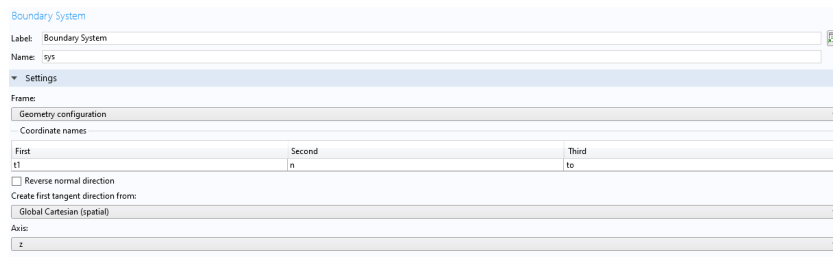
(a) 1: the parameter definitions



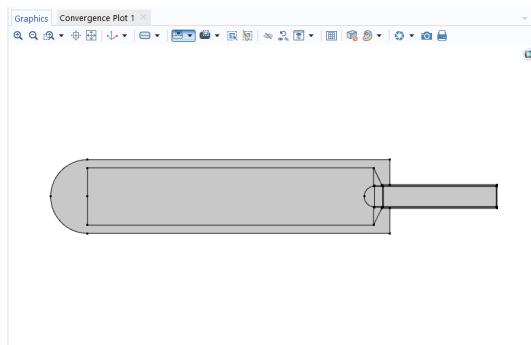
The screenshot shows the 'Global Materials' window in COMSOL Multiphysics. It contains a table with the following data:

| Material  | Selection |
|---|-----------|
| Stainless Steel AISI 316L (mat26)   | Global    |
| Al2O3 (Aluminium sesquioxide, Sapphire, Alumina) (Query 1985: $\hat{\epsilon}$ -Al2O3 (Sapphire); n,k(o) 0.21-... | Global    |
| Edmund optics - Preloaded Nordland - n= 1.52 - abs 320-360 (mat30)  | Global    |
| PMMA resists (Microchem 950 PMMA resist) (mat31)  | Global    |
| Si (Silicon) (Li 1980: n 1.2-14 $\mu$ m; 293 K) (mat32)   | Global    |
| CR-39 (Polymer; n 0.58929 $\mu$ m) (mat33)  | Global    |

(b) 2: Material overview



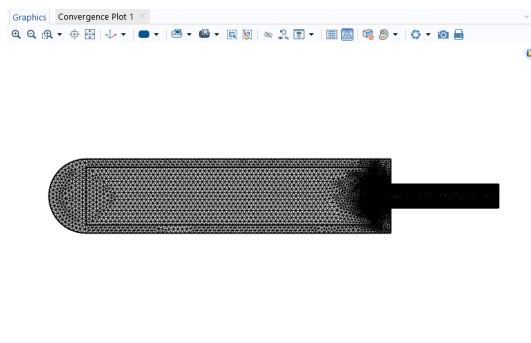
(c) 3: Boundary system



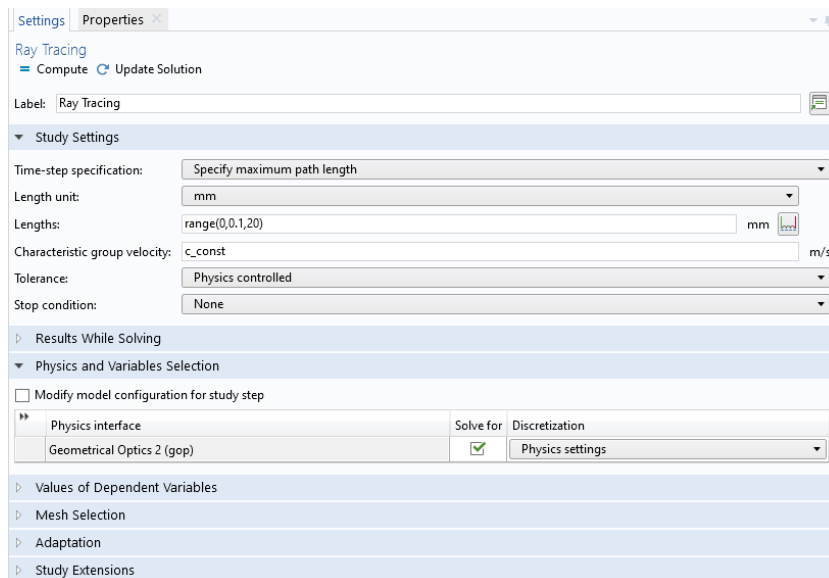
(d) 4: Geometry of the assembly

- Geometrical Optics 2 (gop)
  - Medium Properties 1
  - Material Discontinuity 1
  - Ray Properties 1
  - Ray Termination 1
  - Release from Grid 1
  - Release from Grid 2
  - Release from Grid 3
  - Ray Detector 1
  - Material Discontinuity 3
  - Material Discontinuity 4
  - Mirror 1
  - Wall 1
  - Equation View

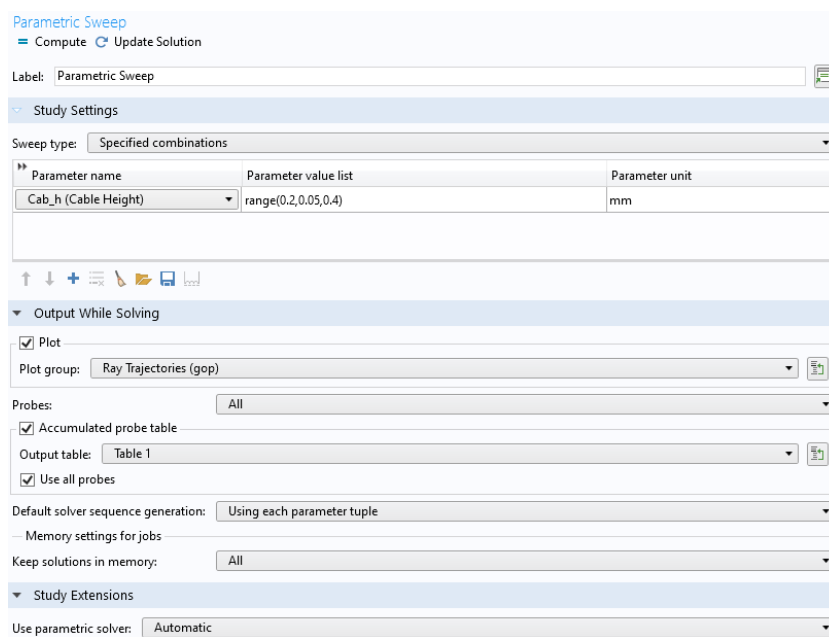
(e) 5: Study:Geometrical Optics



(f) 6: Mesh of the assembly



(g) 7: simulated Ray tracing



(h) 8: simulated Parametric sweep

Figure C.1: The COMSOL steps taken for the encapsulated optical *in vivo* dosimetry (OIVD) sensor assembly with the  $ZnSe:O$  scintillator and the silica-doped fibre by CeramOptec.



# D

## MATLAB Scripts

The relevant MATLAB scripts are printed in this appendix to give more insight into the data processing. These scripts are not copied directly: some administrative lines were removed to improve the readability of this report.

### D.1. Parameter sweep analysis

```
1 function out = model
2
3 import com.comsol.model.*
4 import com.comsol.model.util.*
5
6 model = ModelUtil.create('Model');
7 model.component.create('comp1', true);
8
9 model.component('comp1').geom.create('geom1', 2);
10 model.component('comp1').geom('geom1').axisymmetric(true);
11
12 model.component('comp1').mesh.create('mesh1');
13
14 model.component('comp1').physics.create('gop', 'GeometricalOptics', 'geom1');
15
16 model.study.create('std1');
17 model.study('std1').create('rtrac', 'RayTracing');
18 model.study('std1').feature('rtrac').activate('gop', true);
19
20 model.component('comp1').geom('geom1').create('r1', 'Rectangle');
21 model.component('comp1').geom('geom1').feature('r1').set('size', {'Sci_l' 'Sci_h'});
22
23 model.param.set('Sci_l', '0.7[mm]');
24 model.param.set('Sci_h', '3.5[mm]');
25 model.param.descr('Sci_l', 'Scintillator Length');
26 model.param.descr('Sci_h', 'Scintillator Height');
27
28 model.component('comp1').geom('geom1').run('r1');
29 model.component('comp1').geom('geom1').feature('r1').set('size', {'Sci_w' 'Sci_h'});
30
31 model.param.rename('Sci_l', 'Sci_w');
32 model.param.set('Sci_w', '3.5[mm]');
33 model.param.set('Sci_h', '0.7[mm]');
34
35 model.component('comp1').geom('geom1').run('fin');
36
37
38 model.param.set('Lens_r', '0.35[mm]');
39 model.param.descr('Lens_r', 'Radius Lens');
40
41 model.component('comp1').geom('geom1').feature('c1').set('r', 'Lens_r');
42 model.component('comp1').geom('geom1').run('c1');
43 model.component('comp1').geom('geom1').feature('r2').set('size', {'Cab_w' 'Cab_l'});
```

```

44
45 model.param.set('Cab_w', '3.5[mm]');
46 model.param.descr('Cab_w', 'Cable Length');
47 model.param.descr('Sci_w', 'Scintillator Length');
48 model.param.set('Cab_h', '0.1[mm]');
49 model.param.descr('Cab_h', 'Cable Hight');
50
51 model.component('comp1').geom('geom1').run('c1');
52 model.component('comp1').geom('geom1').feature('r2').set('size', {'Cab_w' 'Cab_h'});
53 model.component('comp1').geom('geom1').run;
54
55 model.sol('sol1').study('std1');
56
57 model.study('std1').feature('rtrac').set('notlistsolnum', 1);
58 model.study('std1').feature('rtrac').set('notsolnum', '1');
59 model.study('std1').feature('rtrac').set('listsolnum', 1);
60 model.study('std1').feature('rtrac').set('solnum', '1');
61
62 model.sol('sol1').feature.remove('t1');
63 model.sol('sol1').feature.remove('v1');
64 model.sol('sol1').feature.remove('st1');
65 model.sol('sol1').create('st1', 'StudyStep');
66 model.sol('sol1').feature('st1').set('study', 'std1');
67 model.sol('sol1').feature('st1').set('studystep', 'rtrac');
68 model.sol('sol1').create('v1', 'Variables');
69 model.sol('sol1').feature('v1').set('control', 'rtrac');
70 model.sol('sol1').create('t1', 'Time');
71 model.sol('sol1').feature('t1').set('tlist', 'range(0,0.01,1)');
72 model.sol('sol1').feature('t1').feature.remove('fcDef');
73 model.sol('sol1').attach('std1');
74 model.sol('sol1').runAll;
75
76
77 model.component('comp2').physics('gop2').feature('op1').set('RayPropertySpecification', ..
    ↪ 'SpecifyVacuumWavelength');
78
79 model.label('MATLAB_OIVD.mph');
80 model.component('comp2').physics('gop').feature('mir1').active(true);
81 model.component('comp2').geom('geom2').run;
82
83 out = model;

```

## D.2. Seed points for the scintillator

```

1 Sci_w_mm = 3.5; %mm
2 Sci_w = Sci_w_mm/1000;%m
3
4 Sci_h_mm=0.7; %mm
5 Sci_h =Sci_h_mm/1000; %m
6 % Scintillation Crystal 3D
7
8 p1=[0.0, 0.0, 0];
9 p2=[0.0, 0.0, Sci_w];
10 R=Sci_h/2;
11 N = 100; % # seeding points
12
13 axialvec = p2 - p1;
14 axialvec = axialvec/norm(axialvec);
15 axialpoints = p1 + (p2 - p1).*rand(N,1);
16
17 circr = sqrt(rand(N,1))*R;
18 circtheta = rand(N,1)*2*pi;
19 circpoints = [cos(circtheta).*circr,sin(circtheta).*circr];
20
21 %Rotate the points into the plane perpendicular to the axis.
22
23 axnull = null(axialvec);
24 points3D = axialpoints + circpoints*axnull.';

```



```
25 points2D = points3D(:, [3,1]);
26
27 %And plot.
28
29 plot3(points3D(:,1),points3D(:,2),points3D(:,3),'.')
30 grid on
31 box on
32 axis equal
33
34 figure
35
36 plot(points2D(:,1),points2D(:,2),'.')
37 grid on
38 box on
39 axis equal
40
41 % Write data to text file
42 dlmwrite('SeedPoints_100_3D.txt',points3D)
43 dlmwrite('SeedPoints_100_2D.txt',points2D)
```